The Key Role of Warm Rain Parameterization in Determining the Aerosol Indirect Effect in a Global Climate Model

XIANWEN JING AND KENTAROH SUZUKI

Atmosphere and Ocean Research Institute, The University of Tokyo, Kashiwa, Japan

TAKURO MICHIBATA

Research Institute for Applied Mechanics, Kyushu University, Fukuoka, Japan

(Manuscript received 15 November 2018, in final form 18 April 2019)

ABSTRACT

Global climate models (GCMs) have been found to share the common too-frequent bias in the warm rain formation process. In this study, five different autoconversion schemes are incorporated into a single GCM, to systematically evaluate the warm rain formation processes in comparison with satellite observations and investigate their effects on the aerosol indirect effect (AIE). It is found that some schemes generate warm rain less efficiently under polluted conditions in the manner closer to satellite observations, while the others generate warm rain too frequently. Large differences in AIE are found among these schemes. It is remarkable that the schemes with more observation-like warm rain formation processes exhibit larger AIEs that far exceed the uncertainty range reported in IPCC AR5, to an extent that can cancel much of the warming trend in the past century, whereas schemes with too-frequent rain formations yield AIEs that are well bounded by the reported range. The power-law dependence of the autoconversion rate on the cloud droplet number concentration β is found to affect substantially the susceptibility of rain formation to aerosols: the more negative β is, the more difficult it is for rain to be triggered in polluted clouds, leading to larger AIE through substantial contributions from the wet scavenging feedback. The appropriate use of a droplet size threshold can mitigate the effect of a less negative β. The role of the warm rain formation process on AIE in this particular model has broad implications for others that share the too-frequent rain-formation bias.

1. Introduction

The aerosol indirect effect (AIE) is of great importance in regulating the global energy budget. It is generally perceived that an increase in atmospheric cloud-active aerosols, such as anthropogenically emitted sulfate aerosols, acts to increase the numbers and decrease the sizes of cloud droplets for a given cloud water amount, making the clouds more reflective to shortwave radiation (Twomey 1977); this is known as the "albedo effect." On the other hand, the reduction in cloud particle sizes can inhibit the formation of precipitation due to the less efficient collision and coalescence of cloud droplets, so as to influence the lifetime and cover of clouds (Albrecht 1989; Kaufman and Koren 2006), known as the "lifetime effect." While some intrinsic microphysical or macrophysical mechanisms can buffer (i.e., mitigate) the albedo and lifetime effects (Stevens and Feingold 2009; Small et al. 2009), it is generally accepted that the net effect of AIE is to cool the surface temperature and partially offset greenhouse gas warming (Boucher et al. 2013).

Given the importance of AIE to Earth's energy budget and the large anthropogenic contribution to the atmospheric aerosols in the industrial era, it has been a major interest of many studies to estimate the AIE from the preindustrial (PI) to the present-day (PD) period

Denotes content that is immediately available upon publication as open access.

Supplemental information related to this paper is available at the Journals Online website: https://doi.org/10.1175/JCLI-D-18-0789.s1.

Corresponding author: Xianwen Jing, jing_xw@aori.u-tokyo.ac.jp

DOI: 10.1175/JCLI-D-18-0789.1

(Knutti et al. 2002; Wilcox et al. 2013; Stevens 2015; Zhang et al. 2016). However, significant inconsistency exists among the AIE estimates of global climate models (GCMs) (Boucher et al. 2013), indicating a substantial discrepancy in the sensitivity of Earth's energy budget to aerosol perturbations among GCMs. This has been found to be a dominant factor that led to the diversity in the simulated surface mean temperature in the CMIP5 models (Rotstayn et al. 2015), and also a major source of uncertainties for the projections of climate in the near decades (Collins et al. 2013). For this reason, increasing studies have been endeavoring to disentangle the complexity of the multiple processes operating in AIE from the observational sector (Rosenfeld et al. 2014; Malavelle et al. 2017; Ma et al. 2018), or to constrain and improve the representations of these processes in GCMs (Wang et al. 2012; Fan et al. 2013; Donner et al. 2016; Rothenberg et al. 2018; Sullivan et al. 2018).

One particular process that is closely associated with AIE is the production of precipitation, which both depletes cloud water and also deposits aerosols. Previous studies have demonstrated that modifications to the representation of precipitation could give rise to large variations in simulated AIE (e.g., Rotstayn 2000; Golaz et al. 2011). For instance, the simulated AIE in the GFDL CM3 model was found to be linearly related to the threshold of droplet effective radius R_e for the onset of precipitation (Golaz et al. 2011); in some other models, the shifting from the diagnostic to the prognostic representation of precipitation substantially reduced the AIE due to the shift of the emphasis of rain production from the autoconversion process to the accretion process for the prognostic approach (Posselt and Lohmann 2009; Michibata et al. 2019). These studies suggest that no consensus about the treatment of precipitation has been reached among GCMs and that a promising approach to constrain AIE for GCMs is to reconcile the modeled precipitation process with observations.

Despite the fact that the global-mean surface precipitation amounts simulated by state-of-the-art GCMs are generally close to observations since they are largely controlled by energy budgets constraints (Suzuki et al. 2017), a number of them have been found to generate precipitation too frequently and too lightly (Stephens et al. 2010; Hill et al. 2015; Jing et al. 2017). Process-level evaluations of the precipitation formation process in such models revealed that they commonly initiate precipitation, especially warm rain (i.e., rain in warm-topped clouds), in clouds with both cloud water amount and cloud droplet sizes much smaller than occurred in the observations (Suzuki et al. 2015; Jing et al. 2017). That is, warm rain formation in such models starts too easily when cloud microphysical properties cannot sustain such a process in reality. This common defect among some GCMs has a great impact on the simulated AIE as was illustrated by studies with varying R_e thresholds (Golaz et al. 2011, 2013; Suzuki et al. 2013). The key cause of the problem lies in the cloud-to-precipitation transition process, represented as autoconversion parameterization in GCMs. The autoconversion rate R_{aut} is generally formulated as a power-law function of cloud liquid water content L_c and droplet number concentration N_c, in the form of $R_{\text{aut}} \propto L_c^{\alpha} N_c^{\beta}$ (α and β are constants). The formulation of autoconversion controls the timing and efficiency of precipitation formation, and hence should be constrained in order to improve the process-level fidelity of precipitation formation as well as to curtail AIE uncertainty. In particular, the value of β is the critical factor in the formulation since it directly links rain formation to N_c, a quantity highly depending on aerosol conditions.

Continuous and comprehensive measurements of the cloud and precipitation microphysical properties from satellite observations, especially the active detection of cloud vertical structures from *CloudSat* (Stephens et al. 2018), provide detailed insights into the cloud systems on the global scale. These facilitate the investigation of the precipitation process in the context of varying cloud properties (e.g., Suzuki et al. 2010; Nakajima et al. 2010; Takahashi et al. 2017). For instance, it has been demonstrated that the probability density functions (PDFs) of radar reflectively (RR) rescaled as a function of in-cloud optical depth (ICOD), which are then further classified according to cloud-top R_e, can effectively fingerprint the microphysical-structure transition from cloud to rain (Suzuki et al. 2010). This statistic, termed a contoured frequency by optical depth diagram (CFODD), has been employed to expose the processes-level biases in the warm rain formation processes of various GCMs (Suzuki et al. 2015; Jing et al. 2017).

Although it is well acknowledged that the precipitation treatments in models have great impacts on the simulated precipitation and AIE, it is not yet adequately understood how they affect the process-level behavior of precipitation, and even less is known about how the process-level behavior of precipitation propagates to the AIE through its correlation with cloud microphysics as well as the interplay with aerosols. Specially, as mentioned above, the autoconversion process that governs the onset of warm rain is of primary importance to the characteristics of the precipitation process. Jing and Suzuki (2018, hereinafter JS18) compared two distinct autoconversion schemes in a single GCM against satellite observations in their representations of the warm rain process and revealed that the

differing autoconversion processes affect AIE through the varying sensitivities of cloud water response to aerosol perturbations, which could be amplified through the wet scavenging feedbacks to the extent depending on the autoconversion formulations. This study extends the previous work to include a wide range of autoconversion representations in the literature, which will illustrate whether the findings by JS18 can generally apply to other autoconversion schemes, and also allows for more systematic investigation of the key factors in the autoconversion formulations that determine the characteristics of warm rain intensity and frequency, and hence the consequent AIE.

Five widely used autoconversion schemes that employ largely different functional forms of formulations are incorporated into a single model here. Our major objectives are 1) to evaluate the precipitation formation processes represented by the various autoconversion schemes in comparison with satellite observations and to clarify how the differing representations of precipitation affect their features in the aerosol–cloud interaction, and 2) to quantify the impacts of the varying autoconversion formulations on the AIE from the PI to PD period and to explore the pathways through which the differences in the precipitation formation process propagate to the AIE. Special interest is put on the effect of varying values of β.

The model and observational data used in this study, as well as the experimental setups, are described in section 2. Section 3, utilizing the simulations for the PD period, evaluates the precipitation formation processes of the various schemes against satellite observations. This serves as a basis for analyzing the interaction between precipitation and cloud/aerosols in terms of the susceptibilities to aerosol environment. The impacts of the alternating autoconversion schemes on the AIE are investigated in section 4, with a particular emphasis on the effect of β and wet scavenging feedback. Section 5 gives the conclusions and discussion.

2. Model, data, and experiments

a. Model description

The atmospheric version of the Model for Interdisciplinary Research on Climate version 5.2 (MIROC5.2) (Watanabe et al. 2010), jointly developed at the Atmosphere and Ocean Research Institute of the University of Tokyo, the National Institute for Environmental Studies, and the Japan Agency for Marine-Earth Science and Technology, is used in this study. The model has a standard horizontal resolution of T85 (~1.4°) and a vertical resolution of 40 layers up to about 3 hPa.

Full aerosol–cloud interactions are considered by incorporating the Spectral Radiation-Transport Model for Aerosol Species (SPRINTARS) (Takemura et al. 2000, 2002), in which all the main tropospheric aerosol types and their precursors are included. The wet scavenging rates of the various aerosol species are parameterized as functions of precipitation fluxes and aerosol microphysical properties such as number concentration and radius (Takemura et al. 2000), and hence the wet scavenging efficiencies are highly amenable to precipitation changes. The number concentrations of both water droplets (Abdul-Razzak and Ghan 2000) and ice crystals (Takemura et al. 2009) are prognostic variables in the two-moment bulk microphysics and are coupled with the radiation and precipitation schemes.

The warm rain formation scheme of the standard MIROC5.2 is from Berry (1968). Four alternative schemes that have been widely used in other models are also incorporated into MIROC5.2 (Michibata and Takemura 2015). The formulations of the autoconversion rate $R_{\rm aut}$ ($\mathrm{kg\,m^{-3}\,s^{-1}}$) for the five schemes employed in this study are as follows:

1) Berry (1968):

$$R_{\rm aut} = \frac{3.5\times10^{-2}L_c^2}{0.12+1.0\times10^{-12}\dfrac{N_c}{L_c}}, \tag{1}$$

2) Tripoli and Cotton (1980):

$$R_{\rm aut} = f_{\rm tune}\times\frac{0.104gE_{\rm cr}}{\mu\rho_w^{1/3}}L_c^{7/3}N_c^{-1/3}H(q_c-q_{\rm crit}), \tag{2}$$

3) Liu and Daum (2004):

$$R_{\rm aut} = f_{\rm tune}\times\left(\frac{3}{4\pi\rho_w}\right)^2\kappa_2\beta_6^6L_c^3N_c^{-1}H(R_6-R_{6c}), \tag{3}$$

4) Khairoutdinov and Kogan (2000):

$$R_{\rm aut} = f_{\rm tune}\times1350\times L_c^{2.47}(N_c\times10^{-6})^{-1.79}\rho_a^{-1.47}, \quad \text{and} \tag{4}$$

5) Beheng (1994):

$$R_{\rm aut} = f_{\rm tune}\times6.0\times10^{28}n^{-1.7}(L_c\times10^{-3})^{4.7}(N_c\times10^{-6})^{-3.3}, \tag{5}$$

where the units of L_c and N_c are $\mathrm{kg\,m^{-3}}$ and $\mathrm{m^{-3}}$, respectively; ρ_a and ρ_w are the air and water density ($\mathrm{kg\,m^{-3}}$), respectively; H denotes the Heaviside step function with a threshold cloud water mixing ratio [Eq. (2)] or droplet effective radius [Eq. (3)]. Note that $f_{\rm tune}$ is a tuning factor introduced here to bring the TOA

TABLE 1. The values of α and β in the autoconversion formulation $R_{aut} \propto L_c^{\alpha} N_c^{\beta}$ for each scheme; β^* are artificially varied values of β designated for AIE sensitivity tests.

	BR68	TC80	LD04	KK00	BH94
α	~3	7/3	3	2.47	4.7
β	~−1	−1/3	−1	−1.79	−3.3
β^*	~−1.2	−2/3	−1/3	−1/3	−1/3

energy budget to an amount comparable to the default BR68 simulation (targeting $\pm 0.5\,\mathrm{W\,m^{-2}}$ for the PD simulations). This tuning approach alters the magnitude of R_{aut} without changing the functional dependency of R_{aut} on L_c and N_c, which cover a wide range among these schemes (the values of α and β in $R_{aut} \propto L_c^{\alpha} N_c^{\beta}$ for each scheme are listed in Table 1). Other parts of the model are held exactly the same. For convenience, the above autoconversion schemes [Eqs. (1)–(5)] will be referred to as BR68, TC80, LD04, KK00, and BH94, respectively.

To facilitate consistent comparisons with satellite observations, the Cloud Feedback Model Intercomparison Project Observation Simulation Package (COSP) version 2.0 (Swales et al. 2018) is implemented in MIROC5.2 to translate the model cloud fields into observation-like signals or retrievals at subcolumns defined within the model grids. Here the number of subcolumns in each grid point is set to 25. COSP has been extensively used for model evaluation and intermodel comparisons (e.g., Lin et al. 2014; Norris et al. 2016; Tsushima et al. 2017; Kay et al. 2018).

b. Observational data

The observational data for the evaluation of warm rain formation process are from the *CloudSat* and *Aqua* satellites that are included in the A-Train constellation. The two satellites pass across a surface footprint within ~1 min (Stephens et al. 2008), such that they can provide near-coincident detections of particular clouds. The *CloudSat* 2B-GEOPROF product (Marchand et al. 2008; http://www.cloudsat.cira.colostate.edu) is employed to provide radar reflectivity profiles within clouds used as an indicator of hydrometeor particle size. The *Aqua* MODIS product (MYD06_L2) (Platnick et al. 2015; https://ladsweb.modaps.eosdis.nasa.gov) collocated to the *CloudSat* footprint provides us with cloud properties used to separate warm (liquid) and cold (ice) clouds and to track the evolution of precipitation: cloud-top temperature T_{ctop}, cloud-top R_e, and cloud optical depth τ_c. The observations during 2007–10 are used here.

Additional data are employed for the purpose of evaluating the simulated PD climates. These include the cloud fraction from the MODIS *Aqua* and *Terra* combined cloud product MCD08_M3 intended for model evaluations (Pincus et al. 2012; http://climserv.ipsl.polytechnique.fr/cfmip-obs.html); the aerosol optical depth (AOD) from the Level-3 (L3) MODIS Atmosphere Monthly Global Product MYD08_M3 (Platnick et al. 2017; https://dx.doi.org/10.5067/MODIS/MYD08_M3.006); the liquid water path (LWP) from the Multisensor Advanced Climatology of Liquid Water Path (MAC-LWP) dataset (Elsaesser et al. 2017; https://disc.gsfc.nasa.gov); the surface precipitation rate from the Global Precipitation Climatology Project monthly precipitation dataset (GPCP) (Adler et al. 2003; https://www.esrl.noaa.gov/psd); and the TOA radiation budgets (including cloud radiative forcing) from the CERES EBAF-TOA Ed4.0 product (Loeb et al. 2018; https://ceres.larc.nasa.gov).

c. Experiments

Two main sets of experiments are performed to address the objectives of this study. First, to understand the process-level behavior of warm rain formation, a 1-yr simulation under the PD aerosol emissions is conducted for each autoconversion scheme; the results are saved as 6-hourly snapshots such that the instantaneous cloud microphysical properties can be used to construct statistics that are directly comparable to the satellite-based metric. The RR from the *CloudSat* cloud profile radar simulator and the τ_c from the MODIS simulator, both embedded in the COSP, are applied to facilitate the model–satellite comparisons.

Second, in order to assess the impact of the various autoconversion formulas on the AIE, a pair of 11-yr simulations under the PI and PD aerosol emissions, represented by the estimates for the years 1850 and 2000 from the representative concentration pathways dataset (van Vuuren et al. 2011), respectively, are conducted for each autoconversion scheme. Prescribed sea surface temperature (SST) and constant greenhouse gases are employed. Since all model setups are consistent between the PI and PD runs except for the aerosol emissions, the PD − PI differences indicate the aerosol-induced changes to the simulated climate. The comparisons among the various schemes will imply the role of precipitation formation process on modulating the simulated PD − PI climate changes and AIEs.

The sensitivity of AIE and cloud properties to the choice of β is tested for each scheme, with an artificially altered value of β. The newly designated values of β are listed in Table 1. The choice of these values is meant to cover the multischeme range of β as much as possible without a breakdown of the run. We also examined the effect of using a R_e threshold on AIE for the LD04 scheme. These tests are also run for 11 model years under the PD and PI aerosol conditions.

In addition, the climate sensitivity λ [K $(\mathrm{W\,m^{-2}})^{-1}$]—that is, the response of global-mean surface temperature to unit radiative forcing at the TOA—is calculated for each of the various model constructions, such that it is straightforward to translate the above AIEs into possible changes in global-mean surface temperature from PI to PD. It has been shown in previous studies that AIE is equally efficient in altering surface temperature compared to CO_2 forcing (Hansen et al. 2005), but the efficacy may vary with climate state. Two 6-yr simulations are conducted with the SST universally increased and decreased by 2 K based on the climatological July SST data, respectively; and λ is calculated from $\lambda = \Delta T/\Delta F$ (Cess et al. 1990), where ΔT and ΔF are the differences in the global-mean TOA net radiation flux and surface temperature, respectively, between the two simulations.

We also make further investigation to the impacts of the wet scavenging feedback on AIE for the five autoconversion schemes. JS18 has found that the changes in the precipitation formation process result in differences in the efficiency of wet scavenging, which in turn feedback on cloud microphysics and precipitation. This study extends this analysis into the various autoconversion schemes for more systematic estimates of this contribution from the wet scavenging. An extra pair of PI and PD simulations for each scheme are conducted, in which an additional precipitation flux especially for the wet scavenging process is calculated with fixed N_c, while the precipitation flux calculated using aerosol-mediated N_c remains for the cloud–precipitation interaction. Since N_c is the pathway through which aerosols can affect precipitation, this treatment turns off the connection between the aerosol-mediated precipitation and the wet scavenging process, thereby removing the feedback on AIE from the wet scavenging. The fixed N_c is set to the intermediate value $3.0 \times 10^7\,\mathrm{m^{-3}}$; the use of different values typical in the model's N_c spectrum can affect the specific values of the AIEs, but not the main conclusions about the relative importance of wet scavenging feedback in modulating AIE (JS18).

3. PD warm rain formation processes

a. PD climate states

Before examining the process-level behaviors of the warm rain formation processes, we first compare the PD climate states by using the various autoconversion schemes. Figure 1 shows the multiyear zonal means of the variables about the clouds, aerosols, precipitation, and energy budget from the PD simulations, as well as from the corresponding observations. The global-mean values of both the PD and PI simulations, as well as the comparison to available observations, are shown in Table 2.

In general, the simulated climate states, especially the surface precipitation rate P (Fig. 1c) and the TOA radiative fluxes (Figs. 1e–h), are very close to each other; the interscheme differences are much smaller than those between the model simulations and observations. This is because the prescribed climatological SST limits the variation in mean climate between the simulations. The most notable variations among the model simulations occur for LWP (Fig. 1b) and AOD (Fig. 1d); the BR68 and TC80 schemes feature relatively smaller LWP and AOD than do the other schemes. The global-mean differences in LWP and AOD among the various schemes are $17\,\mathrm{g\,m^{-2}}$ (~30%) and 0.019 (~19%), respectively. These variations in LWP and AOD reflect the impacts of the autoconversion formulations on the depletion of cloud water and wet scavenging of aerosols by precipitation, which will be examined in detail in the following subsections. The considerable differences in LWP cause only moderate differences in cloud radiative forcing (Figs. 1e,f), within $1\,\mathrm{W\,m^{-2}}$ in terms of the global mean; this is because the schemes with larger LWP also have smaller cloud fraction, which compensate for part of the radiative effects of the thickened clouds.

Figure 1 and Table 2 suggest that most variables in the PD simulations are analogous to each other among the various schemes, except for the properties of clouds and aerosols (e.g., LWP and AOD), which are directly modulated by the different autoconversion formulations. Therefore, the abilities of the model to reproduce the present-day climate states do not change notably by altering the autoconversion process.

b. Warm rain formation process

The aforementioned CFODD method is applied to assess the characteristics of the warm rain formation processes in comparison with the A-Train observations. The PDFs of RR (classified into 25 bins ranging from −30 to 20 dBZ) are computed and normalized at each ICOD bin (15 bins are used here from 0 to 60) for each of the three cloud-top R_e ranges (R_e = 5–10, 10–15 and 15–20 μm, respectively), for single-layer warm clouds only ($T_{\mathrm{ctop}} > 273.15$ K), and then displayed in the form of contoured frequency diagrams. For observations, the vertical profiles of ICOD are determined from the MODIS τ_c with an adiabatic growth assumption algorithm (Suzuki et al. 2010). For models, the RRs are from the *CloudSat* simulator (Haynes et al. 2007) involved in COSP, and the ICOD profiles are computed using the τ_c from the MODIS simulator and the same adiabatic growth algorithm.

Figure 2 shows that the observed RR shifts monotonically from small (RR < −15 dBZ; Fig. 2a) to larger values (RR > 0 dBZ; Fig. 2c) with increasing R_e at the lower parts (ICOD > 40) of the diagrams.

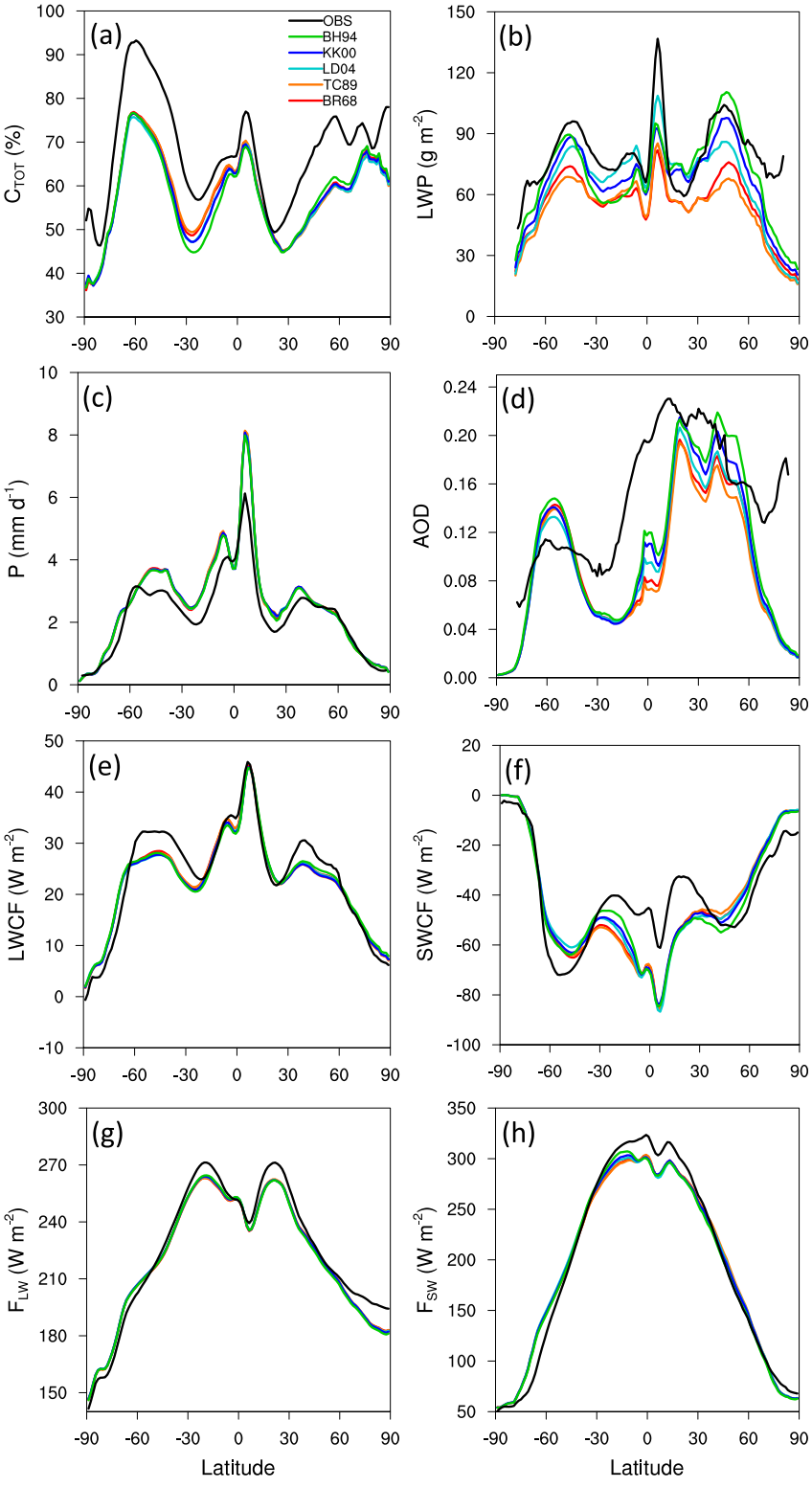

FIG. 1. Zonal means of multiyear averaged (a) cloud fraction, (b) liquid water path (LWP), (c) surface precipitation rate P, (d) aerosol optical depth (AOD), (e) longwave cloud radiative forcing (LWCF), (f) shortwave cloud radiative forcing (SWCF), (g) net longwave flux F_{LW}, and (h) net shortwave flux F_{SW} at the top of the atmosphere for the MIROC5.2 PD simulations and corresponding observations (see the text).

TABLE 2. Global annual means properties from the PI and PD simulations of MIROC5.2 with the five autoconversion schemes, as well as from available PD observations. The numbers in the parentheses are the model–observation differences (first number) and root-mean-square errors (second number). See the text for the observational data used here. The denoted variables and units are as follows: C_{TOT}, total cloud fraction (%); C_{LOW}, low-level cloud fraction (%); C_{MID}, middle-level cloud fraction (%); C_{HGH}, high-level cloud fraction (%); LWP, liquid water path ($g\,m^{-2}$); IWP, ice water path ($g\,m^{-2}$); CDNC, cloud droplet number concentration (m^{-2}); P, surface precipitation rate ($mm\,day^{-1}$); AOD, aerosol optical depth; SH, sensible heat flux; LH, latent heat flux; SWCF, shortwave cloud radiative forcing ($W\,m^{-2}$); LWCF, longwave radiative forcing ($W\,m^{-2}$); SWAF, shortwave aerosol radiative forcing ($W\,m^{-2}$); LWAF, longwave aerosol radiative forcing ($W\,m^{-2}$); F_{SW}, net shortwave radiative flux at the top of the atmosphere (TOA); F_{LW}, net longwave radiative flux at the TOA ($W\,m^{-2}$); F_{NET}, net total radiative flux at the TOA ($W\,m^{-2}$).

	BR68		TC80		LD04		KK00		BH94		
	PI	PD	PI	PD	PI	PD	PI	PD	PI	PD	Obs
C_{TOT}	58.1	58.3 (−8.9, 13.6)	58.2	58.3 (−8.8, 13.7)	56.7	57.4 (−9.8, 14.1)	56.9	57.6 (−9.5, 13.8)	55.8	57.0 (−10.2, 14.2)	67.2
C_{LOW}	29.3	29.4 (−6.0, 9.6)	29.7	29.8 (−5.6, 9.4)	28.2	28.7 (−6.7, 10.0)	28.7	29.2 (−6.2, 9.6)	27.2	28.1 (−7.3, 10.5)	35.4
C_{MID}	7.8	7.9 (−3.1, 8.7)	7.8	7.7 (−3.3, 8.9)	7.7	7.8 (−3.2, 8.8)	7.4	7.5 (−3.5, 8.7)	7.6	7.8 (−3.2, 8.4)	11.0
C_{HGH}	23.7	23.8 (2.7, 6.1)	23.6	23.6 (2.5, 6.1)	23.6	23.6 (2.5, 6.0)	23.4	23.6 (2.5, 6.1)	23.6	23.8 (2.7, 6.1)	21.1
LWP	59.6	60.0 (−20.3, 27.7)	59.0	59.2 (−20.9, 28.1)	70.6	73.3 (−6.6, 19.7)	68.2	71.8 (−8.4, 22.3)	66.0	72.9 (−7.9, 24.1)	82.3
IWP	55.7	56.3	53.5	53.7	64.7	67.6	63.1	67.5	63.0	70.6	—
CDNC	1.73×10^{11}	1.94×10^{11}	1.73×10^{11}	1.92×10^{11}	1.78×10^{11}	2.22×10^{11}	1.74×10^{11}	2.22×10^{11}	1.80×10^{11}	2.45×10^{11}	—
P	3.22	3.21 (0.51, 1.32)	3.23	3.22 (0.52, 1.34)	3.21	3.20 (0.50, 1.31)	3.22	3.21 (0.51,1.32)	3.19	3.18 (0.49, 1.31)	2.70
AOD	0.08	0.11 (−0.05, 0.16)	0.08	0.10 (−0.05, 0.16)	0.08	0.11 (−0.05, 0.16)	0.08	0.11 (−0.04, 0.17)	0.08	0.12 (−0.03, 0.17)	0.16
SH	15.0	14.7	15.0	14.8	15.1	14.8	15.1	14.8	15.2	14.7	—
LH	93.2	92.8	93.5	93.2	93.0	92.7	93.3	92.8	92.4	92.0	—
SWCF	−52.5	−53.4 (−7.6, 19.2)	−52.5	−53.1 (−7.3, 19.9)	−50.3	−52.8 (−7.0, 19.8)	−49.9	−52.5 (−6.7, 18.5)	−48.8	−52.9 (−7.1, 18.4)	−45.8
LWCF	26.4	26.6 (−1.3, 5.3)	26.3	26.4 (−1.5, 5.3)	25.9	26.3 (−1.7, 5.3)	25.8	26.2 (−1.7, 5.5)	25.8	26.4 (−1.6, 5.4)	27.9
SWAF	−0.67	−0.86	−0.68	−0.88	−0.70	−0.86	−0.67	−0.81	−0.69	−0.82	—
LWAF	0.34	0.38	0.34	0.38	0.35	0.39	0.34	0.40	0.36	0.40	—
F_{SW}	237.1	235.6 (−5.6, 19.9)	237.2	235.9 (−5.3, 20.7)	239.5	236.1 (−5.1, 20.5)	239.9	236.2 (−4.9, 19.3)	241.0	235.7 (−5.5, 19.2)	241.2
F_{LW}	−236.5	−236.1 (−4.1, 8.1)	−236.7	−236.4 (−3.8, 7.9)	−237.1	−236.4 (−3.8, 7.9)	−237.2	−236.4 (−3.8, 8.0)	−237.1	−236.1 (−4.1, 8.1)	240.2
F_{NET}	0.66	−0.52 (−1.48, 16.0)	0.52	−0.52 (−1.48, 16.9)	2.37	−0.38 (−1.35, 17.0)	2.71	−0.15 (−1.12, 15.9)	3.88	−0.45 (−1.41, 15.9)	0.96

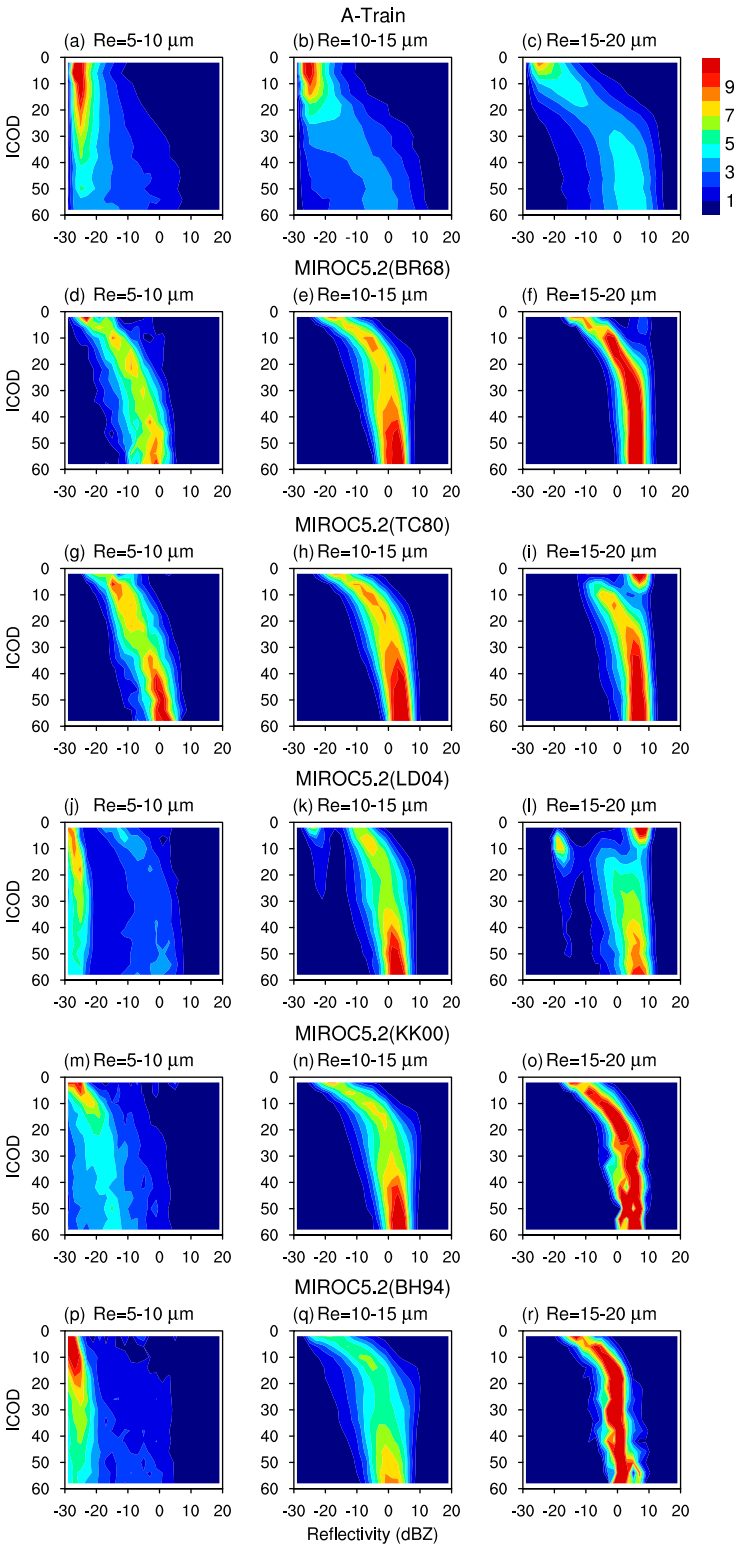

FIG. 2. Normalized probability distribution function of radar reflectivity as a function of ICOD (i.e., CFODD) for (a)–(c) the A-Train observations and (d)–(r) the MIROC5.2 simulations with various autoconversion schemes. The numbers of bins for the ICOD and reflectivity are 15 and 25, respectively.

Clouds with R_e = 10–15 μm feature intermediate RR (-15 dBZ < RR < 0 dBZ). Note that clouds with RR < -15 dBZ, -15 dBZ < RR < 0 dBZ, and RR > 0 dBZ are conventionally regarded as containing nonprecipitating, drizzling (i.e., light rain), and raining (i.e., heavy rain) hydrometeors, respectively (e.g., Haynes et al. 2009). Thus, Figs. 2a–c suggest that precipitation onset is triggered in the R_e range of 10–15 μm, which is also supported by in situ observations (Boers et al. 1998; Pawlowska and Brenguier 2003). If cloud particle sizes are sufficiently small (R_e < 10 μm; Fig. 1a), precipitation is rarely observed even though the cloud optical depth can reach a considerable magnitude. The satellite-based statistics of Figs. 2a–c thus illustrates how the vertical microphysical structure of warm clouds tends to transition from nonprecipitating to precipitating profiles as a fairly monotonic function of the cloud-top particle size.

The transitions of RR profiles with increasing R_e differ greatly among the model simulations with different autoconversion schemes. The results with the BR68 (Figs. 2d–f) and TC80 (Figs. 2g–i) schemes show virtually no nonprecipitating profiles, even for the smallest R_e range, suggesting that rain is formed quite efficiently even when cloud droplet sizes are too small to sustain such an efficient collision and coalescence growth of droplets. Compared with BR68 and TC80, the statistics for R_e = 5–10 μm from the LD04, KK00, and BH94 schemes feature much smaller RR, especially for BH94 (Fig. 2p) which shows the CFODD characteristics most analogous to the A-Train results. These indicate that the cloud-to-precipitation transitions are significantly inefficient in clouds with small droplet sizes for the latter three schemes; such impeded rain formations can be in the polluted regions where the abundant aerosols decrease cloud droplet sizes. It is noticed that there is a somewhat abrupt separation between the nonprecipitating and precipitating profiles for LD04 (Fig. 2j); this stems from the step function dependency of precipitation with a threshold R_e that varies with meteorological conditions. TC80 also adopts a step function representation to trigger precipitation, but the threshold cloud water mixing ratio it employs does not manifest in the R_e-based CFODD diagrams (Figs. 2g–i). For KK00, although the RR values for the smallest R_e range (Fig. 2m) are much smaller than the corresponding BR68 and TC80 results, they are slightly larger than the A-Train observations, implying that drizzle formation is still overestimated in this R_e range under the KK00 scheme. For R_e = 10–15 μm and R_e = 15–20 μm, all schemes overestimate the RR at smaller ICOD (the upper parts of the CFODD diagrams), suggesting that the occurrence of precipitation is too often in clouds with small optical depth (in optically thin clouds or near the cloud top).

Another way to look at the precipitation formation process is the grid-based occurrence frequencies of nonprecipitating, drizzling, and raining clouds (Suzuki et al. 2011; Jing et al. 2017; Kay et al. 2018). The aforementioned criteria (RR < -15 dBZ, -15 dBZ < RR < 0 dBZ, and RR > 0 dBZ) are used to identify nonprecipitating, drizzling, and raining subcolumns, respectively, and the occurrence frequencies of these categories at each grid point are defined as $f_i = N_i/N_{\text{not}}$ (N_{tot} is the total number of cloudy subcolumns; N_i is the number of nonprecipitating/drizzling/raining subcolumns). For satellite observations, this is done by simply counting the originally detected pixels in the grid resolution same as the model. The resultant global distributions of the fractional occurrences are shown in Fig. 3 for both the observations and the model simulations. Note that, for the model results, all subcolumns will be precipitating if there is precipitation occurring in a grid point since there is no information of subgrid precipitation fraction; this is inconsistent with the situation of the A-Train observations in which both precipitating and nonprecipitating pixels can exist within a grid point. To account for this inconsistency, a ''grid-scale'' (GS) calculation of the occurrence frequencies is conducted for ''upscaling'' the observations to the model grid scale—the satellite tracks are latitudinally divided into 1.4°-long segments (each equivalent to a model grid) that are each identified as nonprecipitating, drizzling, or raining according to the maximum RR occurring within the segment (Figs. 3d–f), and counted over time.

The original A-Train data (Figs. 3a–c) show that the majority of the warm clouds are nonprecipitating over broad regions, especially over the continental regions such as East and South Asia, North and South America, Europe, and central Africa, and also over subtropical eastern oceans and midlatitude oceans. Raining warm clouds are more frequently seen over the intertropical convergence zone (ITCZ) (Fig. 3c). The geographical characteristics mostly remains in the grid scale statistics (Figs. 3d,e), except that the magnitudes of the raining-cloud occurrence frequency are increased whereas those of the nonraining clouds are reduced. The global-mean occurrence frequencies of nonprecipitating/drizzling/raining clouds for the original (GS) statistics are 0.53, 0.31, and 0.16 (0.33, 0.31, and 0.36), respectively.

There are remarkable differences among the results of the various autoconversion schemes. Nonprecipitating clouds under the BR68 (Fig. 3g) and TC80 (Fig. 3j) schemes are rarely seen, as has been indicated from the CFODD analysis above. Nonprecipitating clouds under

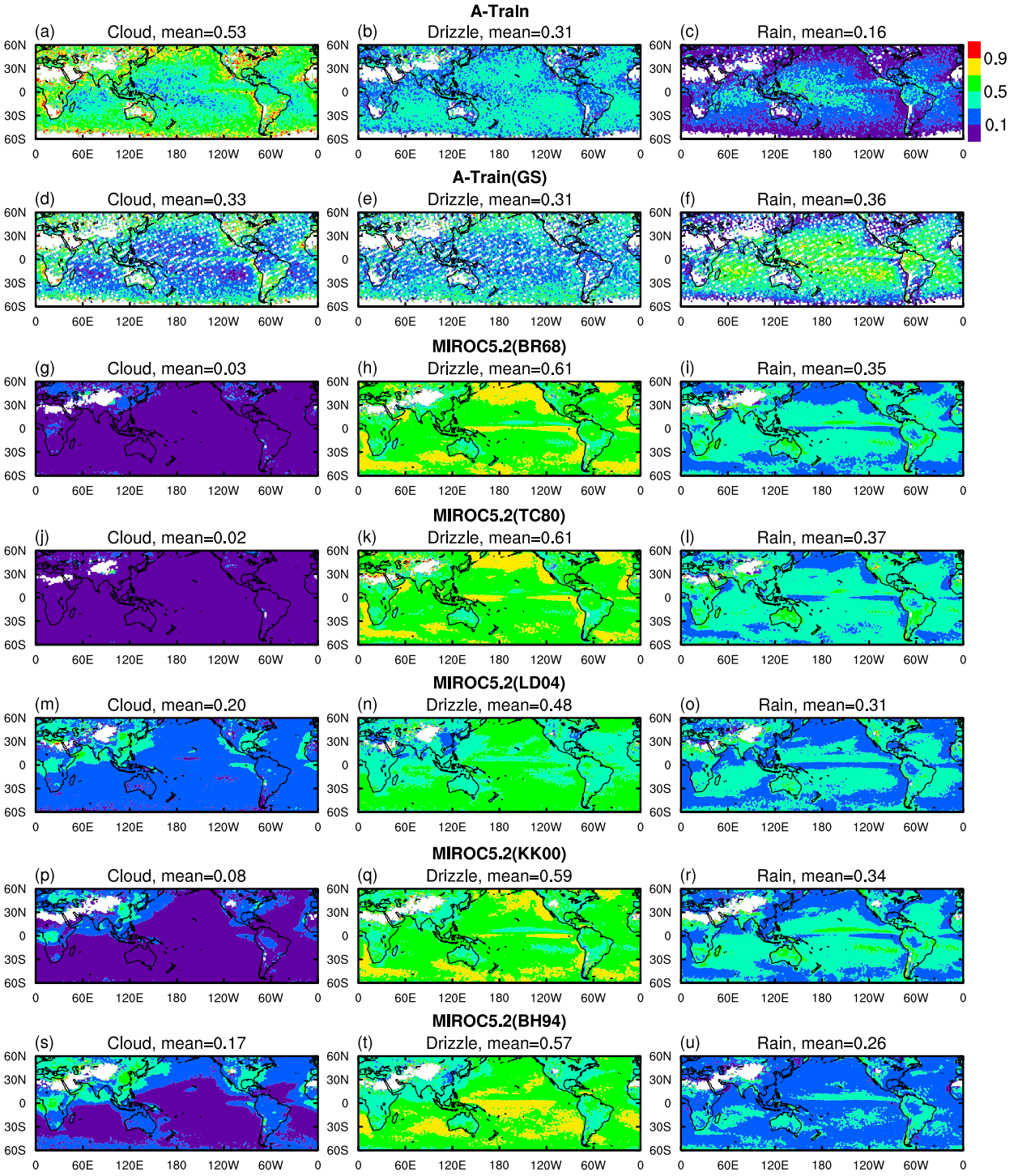

FIG. 3. Distributions of the occurrence frequencies of (left) nonprecipitating clouds ($-30 < \mathrm{RR} < -15$), (center) drizzling clouds ($-15 < \mathrm{RR} < 0$), and (right) raining clouds ($\mathrm{RR} > 0$), defined as N_i/N_{not} (N_{tot} is the total number of cloudy subcolumns; N_i is the number of nonprecipitating/drizzling/raining subcolumns). From top to bottom are the results for the A-Train, A-Train(GS), and MIROC5.2 simulations with the BR68, TC80, LD04, KK00, and BH94 autoconversion schemes, respectively. The satellite statistics are derived on the same grid resolution as those of the model simulations.

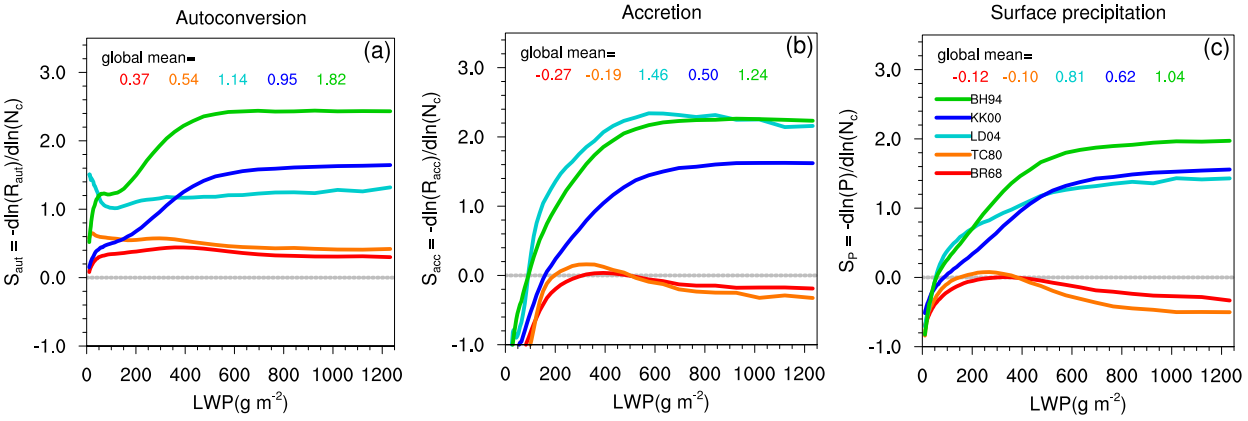

FIG. 4. Susceptibilities of (a) autoconversion rate, (b) accretion rate, and (c) surface precipitation rate to cloud number concentration as a function of LWP for different autoconversion schemes. Also shown are the sample size- and LWP-weighted global-mean values, which are colored as those of the corresponding lines.

the LD04 (Fig. 3m), KK00 (Fig. 3p), and BH94 (Fig. 3s) schemes occur much more frequently than BR68 and TC80 over the continental regions influenced by anthropogenic aerosol loadings, but are still underestimated against satellite statistics over the midlatitude and subtropical oceans to differing extents.

The probability of precipitation in clouds has been shown to be a good indicator of the strength of AIE due to its close correlation with the susceptibility of cloud water to aerosol perturbations (Wang et al. 2012; Bai et al. 2018). Therefore, the occurrence frequencies of nonprecipitating and precipitating clouds shown in Fig. 3 hint at the autoconversion-induced variations in the sensitivity of the warm rain formation process to the aerosol environment, which is assessed in the following subsection.

c. *Microphysical susceptibility to aerosol environment*

We apply the widely used "susceptibility" approach (Jiang et al. 2010; Wang et al. 2012; Michibata et al. 2016; Ma et al. 2018) to depict the sensitivity of the precipitation formation process to the aerosol environment. The aerosol mediated N_c, which reflects the variations in aerosol loadings and also retrievable from satellite remote sensing (Grosvenor et al. 2018), has been widely used in the aforementioned susceptibility assessments. In light of this, we will focus on the susceptibility to N_c in the following analyses.

The susceptibilities of autoconversion rate $R_{\rm aut}$, accretion rate $R_{\rm acc}$, and surface precipitation rate P to N_c are defined respectively as follows:

$$S_{\rm aut} = -d\ln(R_{\rm aut})/d\ln(N_c)|_{\rm LWP}, \quad (6)$$

$$S_{\rm acc} = -d\ln(R_{\rm acc})/d\ln(N_c)|_{\rm LWP}, \quad \text{and} \quad (7)$$

$$S_p = -d\ln(P)/d\ln(N_c)|_{\rm LWP}. \quad (8)$$

With the negative sign in the equations, the physical meaning of the susceptibilities is how efficiently the autoconversion/accretion/surface precipitation is inhibited by increasing aerosols. Figure 4 shows the terms $S_{\rm aut}$, $S_{\rm acc}$, and S_P as a function of LWP for the various schemes, derived from the 1-yr snapshot outputs of the PD simulations. Each number in the figure is based on at least 45 000 valid grid points. The LWP bin boundaries increase geometrically by 10% from 10 to 1291 g m^{-2}. The small LWP bins used here could somewhat limit the effects from the other factors such as meteorological conditions. Figure 4a shows that the differences in $S_{\rm aut}$ among the various schemes are small for LWP $< \sim$100 g m^{-2} and enlarge with increasing LWP. The $S_{\rm aut}$ values for BR68 and TC80 are mostly smaller than the other schemes, and vary only slightly with increasing LWP. In contrast, the LD04, KK00, and BH94 schemes generally show a monotonically increasing $S_{\rm aut}$ with increasing LWP. This behavior can be understood from the autoconversion formulations that are generally written as $R_{\rm aut} \propto L_c^{\alpha} N_c^{\beta}$. Substituting this into Eq. (6), $S_{\rm aut}$ is found to be approximately equal to $-\beta$ for a single layer cloud. We interpret that this control of β on $S_{\rm aut}$ is also manifested in the global, multilayer results of Fig. 4a: the $S_{\rm aut}$ values at larger LWPs reach approximately 0.3, 0.4, 1.2, 1.6, and 2.5 for the TC80, BR68, LD04, KK00, and BH94 schemes, respectively, consistent with the corresponding values of $-\beta$ for these schemes (1/3, ~1.0, 1.0, 1.79, and 3.3, respectively).

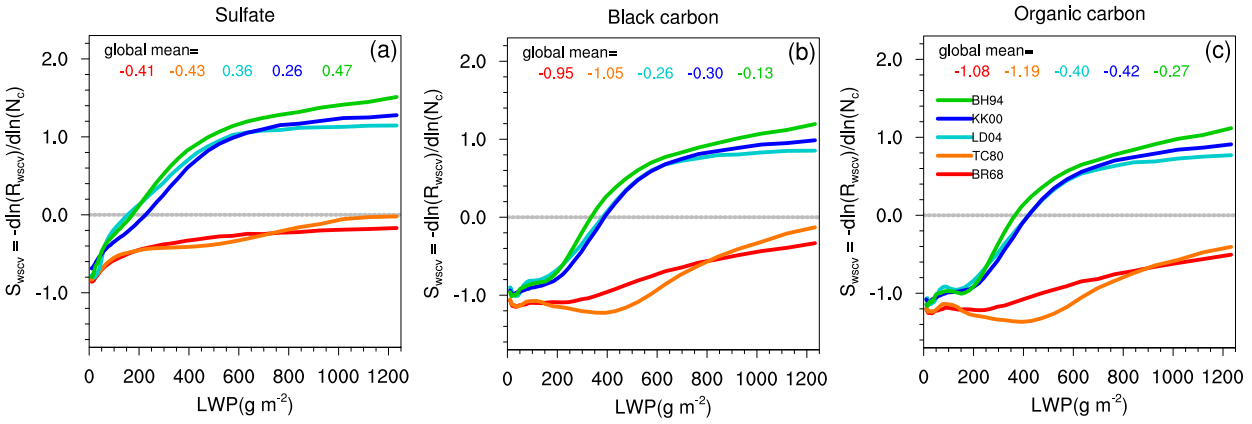

FIG. 5. As in Fig. 4, but for the susceptibilities of aerosol wet scavenging ratio for (a) sulfate, (b) black carbon, and (c) organic carbon.

Although the accretion formulation is set to be common among the various model configurations, S_{acc} is also shown here (Fig. 4b) to investigate how R_{acc} is influenced by the autoconversion process. It can be seen that S_{acc} exhibits somewhat similar features to S_{aut}: the values of S_{acc} for the LD04, KK00, and BH94 schemes increase rapidly with increasing LWP and are mostly larger than those of the BR68 and TC80 schemes. These suggest that the autoconversion parameterizations influence S_{acc} indirectly and significantly through responses of cloud and rainwaters to autoconversion. It is noted that the LD04 scheme shows small S_{aut} dependence on LWP, but much larger S_{acc} dependence on LWP. This is possibly related to the fact that autoconversion works independently at each model layer, whereas accretion is highly associated with the precipitation flux which is vertically accumulated; therefore, the vertical layout of autoconversion (i.e., at which level and at what efficiency the autoconversion is triggered) can also modify the apparent accretion rate. For instance, for a given cloud profile, shifting the triggering of autoconversion to higher levels will expose more cloud water below to the path of rain drops, leaving the LWP to be more important for accretion than for autoconversion.

Negative values of S_{acc} occur at small LWPs for all schemes, and also prevail at LWP $> \sim 500\ \mathrm{g\,m^{-2}}$ for the BR68 and TC80 schemes. The negative values of S_{acc} suggest that the accretion process can be enhanced with increasing aerosols under certain conditions, regardless of the inhibited autoconversion. One possible explanation for the negative S_{acc} is that the initial inhibition of autoconversion-based rain formation could result in an increased cloud water carried over to the following time steps, which may outweigh the autoconversion-induced decrease of the rainwater, leading to an enhanced R_{acc}. This explanation is supported by an additional investigation which shows that the LWP taken to the next step becomes larger with increasing cloud number concentrations (see Fig. S1 in the online supplemental material). Another possibility is that the shift of the onset of autoconversion upward by adding aerosols, implied by elevated precipitation top height with increasing cloud droplet number concentration (CDNC) (Fig. S2), especially when there is less cloud water (i.e., small LWP) to support droplet collision at cloud base, acts to intensify the final accretion rate.

The surface precipitation's susceptibilities to aerosols S_P (Fig. 4c) are the joint result from S_{aut} and S_{acc}. The increasing tendency of S_P with increasing LWP as well as the magnitude of S_P for LD04, KK00, and BH94 are similar to the results obtained from satellite observations (Sorooshian et al. 2009) and fine-resolution model simulations (Feingold et al. 2013), and therefore deemed more realistic. It is also worth noting that the S_P behaviors for the BR68 and TC80 schemes closely resemble the corresponding behaviors of S_{acc}, suggesting that R_{acc} dominates in determining the simulated surface precipitation behavior for these two schemes.

The differences in the precipitation formation process can also affect the wet scavenging efficiencies, and hence the aerosol lifetime (e.g., Textor et al. 2006), in varying aerosol environments. Here, we define the wet scavenging efficiency R_{wscv} as the fraction of aerosols removed from the column aerosol loading by wet scavenging per unit time: $R_{wscv} = A_{wscv}/q_{tot}$, where A_{wscv} and q_{tot} are the wet scavenging flux ($\mathrm{kg\,m^{-2}\,s^{-1}}$) and total aerosol loading ($\mathrm{kg\,m^{-2}}$) in a grid point, respectively. Analogous to Eqs. (6)–(8), we define the susceptibility of R_{wscv} to aerosol perturbations as

$$S_{wscv} = -d\ln(R_{wscv})/d\ln(N_c)|_{LWP}. \quad (9)$$

A positive S_{wscv} indicates that the aerosol removal capability is impeded by increasing aerosols, and vice

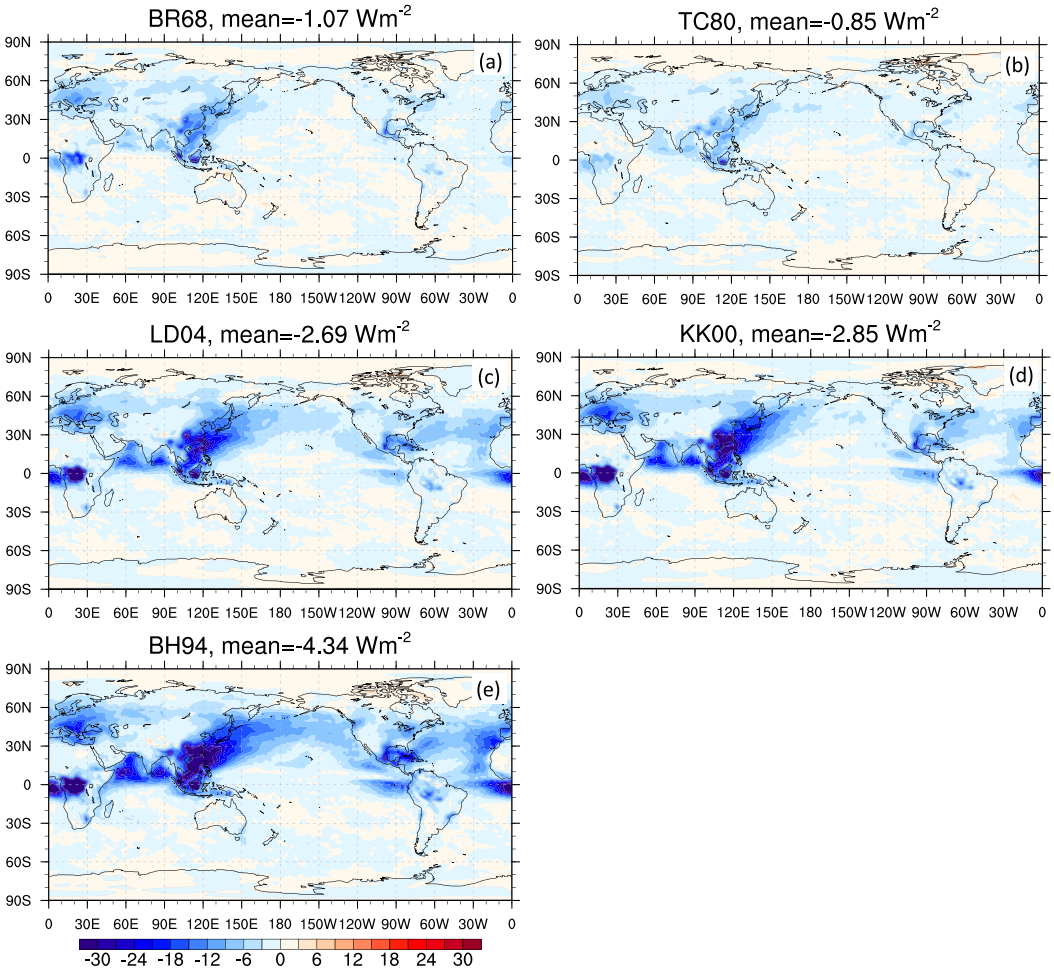

FIG. 6. Global distributions of the AIE from the MIROC5.2 simulations with the (a) BR68, (b) TC80, (c) LD04, (d) KK00, and (e) BH94 autoconversion schemes.

versa. Figures 5a–c show, respectively, the S_{wscv} for the three anthropogenic aerosol species: sulfate (SF), black carbon (BC), and organic carbon (OC). Large deviations are found among the schemes. BR68 and TC80 mostly show negative S_{wscv} although the values become less negative with increasing LWP, while the S_{wscv} for LD04, KK00, and BH94 increase rapidly with LWP and are positive for a moderately large LWP ($>\sim 200\,\mathrm{g\,m^{-2}}$ for SF and $>\sim 400\,\mathrm{g\,m^{-2}}$ for BC and OC). These suggest that, for the latter schemes, increasing aerosols in the atmosphere could impede the R_{wscv} especially when there is an adequate amount of cloud water, leaving more aerosols remaining in the atmosphere. The negative S_{wscv} is probably due to the negative S_{acc}, which enhances subcloud wet scavenging.

These differences in S_{wscv} also protrude in the differences in the AODs of the PD simulations (Fig. 1d and Table 2), in which the schemes with larger (more positive) S_{wscv} also have larger AODs, highlighting the mutual coupling between aerosol and cloud through rain formation and wet scavenging.

4. PD − PI aerosol indirect effect

The analyses above suggest that the various autoconversion schemes can yield analogous PD climate states, but with quite different process-level precipitation behaviors and microphysical susceptibilities to aerosols. In this section, we explore how these differences affect the AIE due to perturbed aerosol emissions from the PI to the PD scenarios.

a. AIE

The method of Ghan (2013) is used to diagnose AIE. It is calculated as $\mathrm{AIE} = \Delta(F_{\mathrm{clean}} - F_{\mathrm{clear,clean}})$. Here, F_{clean} and $F_{\mathrm{clear,clean}}$ are the aerosol-free (calculated by neglecting AOD) all-sky and clear-sky radiative fluxes at the TOA, respectively, and Δ means the PD − PI

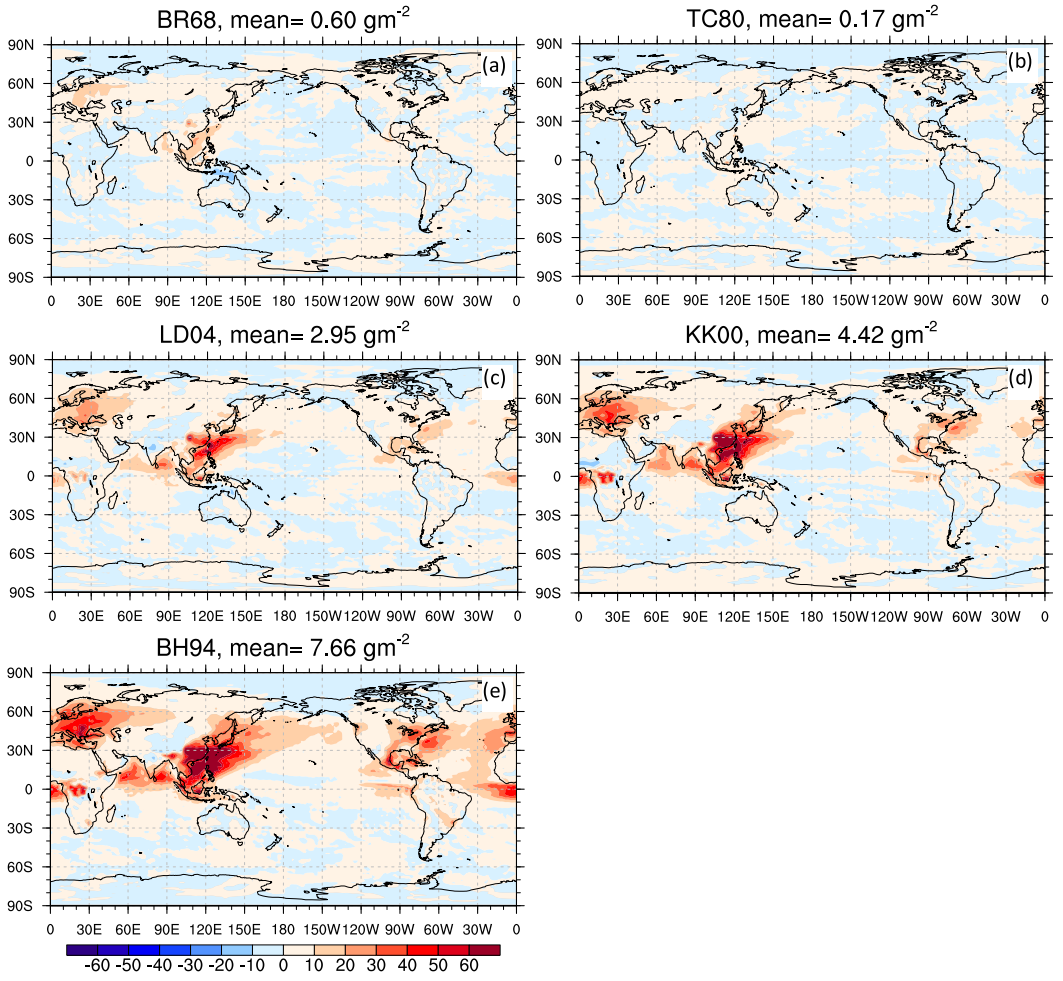

FIG. 7. As in Fig. 6, but for the PD − PI differences in LWP (ΔLWP).

difference. All the fluxes are calculated online by the radiative transfer module. The geographical distributions of AIEs (Fig. 6) show that the AIEs are commonly negative over most regions, particularly over the anthropogenic aerosol source regions over land (e.g., East Asia, central Africa, Europe, and North America) and the surrounding oceans. However, the magnitudes of the AIEs differ greatly especially over the source regions, with global-mean values ranging from -0.85 to $-4.34\,\mathrm{W\,m^{-2}}$. The magnitude and geographical distribution and AIE are highly governed by the regional responses of cloud properties, specifically the increase in LWP and CDNC (Figs. 7 and 8, respectively). Quantitatively, the global-mean ΔLWP and ΔCDNC differ by a factor of as large as about 38 (from ~0.2 to ~7.7 $\mathrm{g\,m^{-2}}$) and 3 (from 0.19×10^{11} to $0.65 \times 10^{11}\,\mathrm{m^{-2}}$), respectively.

The global-mean AIEs are also summarized in Fig. 9 (colored fill), in comparison to the expert judgement in Intergovernmental Panel on Climate Change Fifth Assessment Report (IPCC AR5; Myhre et al. 2013; gray solid fill). The BR68 and TC80 schemes give AIEs within the uncertainty range of the IPCC AR5 judgement while other schemes give too large (negative) AIEs to the extents that are close to (LD04 and KK00) or much larger than (BH94) the effective radiative forcing caused by greenhouse warming for the period 1750–2011 [3.00 (2.22–3.78) $\mathrm{W\,m^{-2}}$] (Myhre et al. 2013), and thus appear to be implausible in the context of explaining historical temperature trend. The standard version of SPRINTARS with the BR68 autoconversion has been found to feature much smaller cloud water response to increasing aerosols than most other models (Ghan et al. 2016); both the previous and this study suggest that the shift to less efficient autoconversion schemes can intensify the cloud water–aerosol connection.

To approximately estimate the historical temperature response to the AIEs thus inferred, we calculate the climate sensitivities λ with the Cess et al. (1990) approach (see section 2c) (Fig. 10). The λ values are close to each

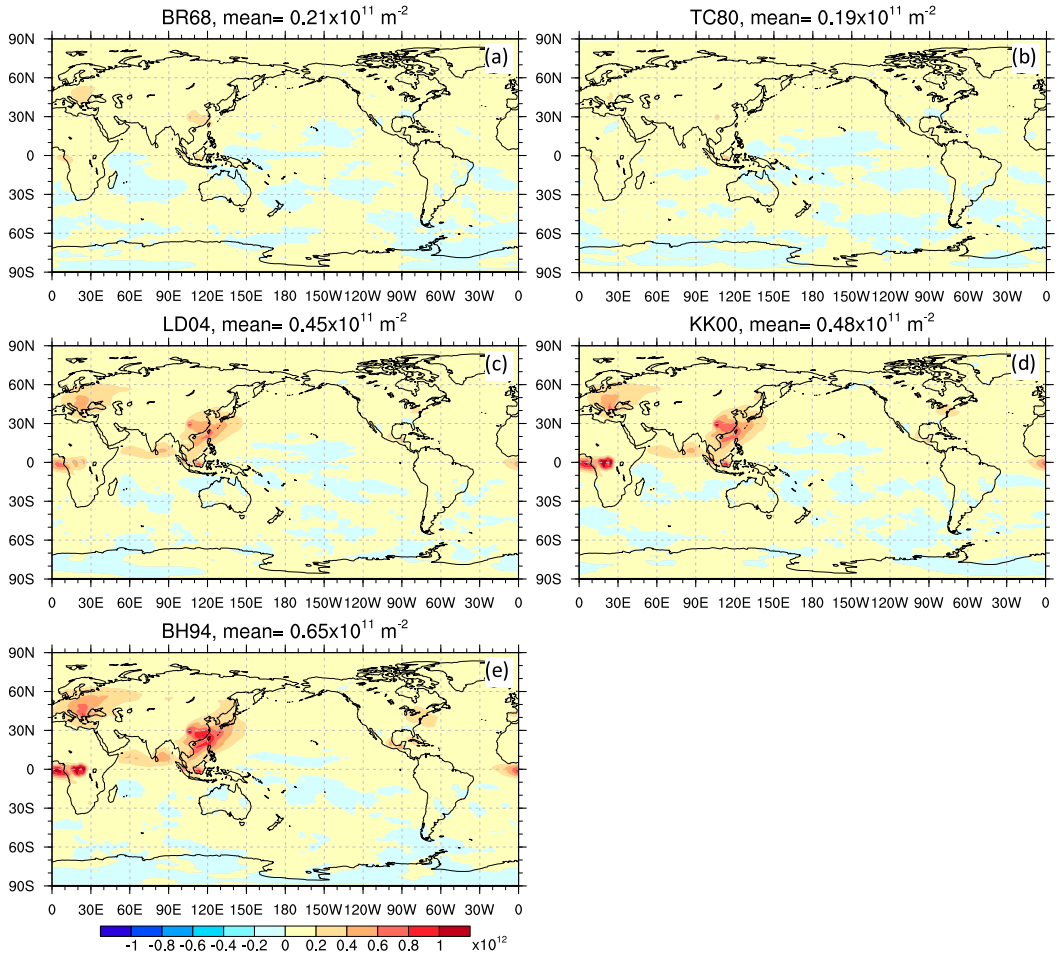

FIG. 8. As in Fig. 6, but for the PD − PI differences in CDNC (ΔCDNC).

other, with a range [0.45–0.49 K $(\mathrm{W\,m^{-2}})^{-1}$] much smaller than those of varying convection schemes in the GFDL AM4 model (Zhao et al. 2016). Given the ΔF (AIE) in Fig. 9 and λ in Fig. 10, we obtain the aerosol-induced change to the surface air temperature ΔT from PI to PD using $\Delta T = \lambda \times \Delta F$ for each scheme as −0.49°C (BR68), −0.38°C (TC80), −1.21°C (LD04), −1.40°C (KK00), and −2.06°C (BH94). The observed trend of surface air temperature showed a global-mean warming of 0.85°C (0.65°–1.06°C) from 1880 to 2012 (Hartmann et al. 2013). Therefore, it is highly probable that the use of the LD04, KK00, and BH94 schemes in full PI-to-PD simulations (with a coupled ocean model) will not capture the warming trend in the past century due to the too-negative AIEs, even though they capture the rain formation process much better than the BR68 and TC80 schemes (Fig. 2). Similar results (i.e., better rain formation but worse historical temperature evolution) have also been found in the GFDL CM3 model (Golaz et al. 2013; Suzuki et al. 2013).

Comparing the precipitation formation processes as illustrated in Fig. 2 and the magnitudes of AIEs, it is found that the CFODD diagrams are not only a good indicator of the precipitation formation process, but also a fairly good indicator of the intensity of the aerosol–cloud interaction—the more robust non-precipitating RR profiles occur in the small R_e range, the more extensively aerosols and clouds interact, and thus larger AIE is generated. Therefore, the precipitation formation process plays a crucial role in determining the strength of AIE in the MIROC5.2 model.

b. *Effect of β*

It has been demonstrated in section 3 that the parameter β used in the autoconversion formulations manifest itself in S_{aut}. To understand the effect of β on AIE, we artificially alter the value of β (Table 1) for each scheme and conduct additional PD and PI simulations.

Figure 11 shows the AIE, ΔLWP, and ΔCDNC as a function of β for each scheme (colored lines). In general, for a particular scheme, the use of smaller β always leads to smaller AIE, due to smaller ΔLWP and ΔCDNC. The interscheme variation in AIE when $-\beta \le 1$ (Fig. 11a) is

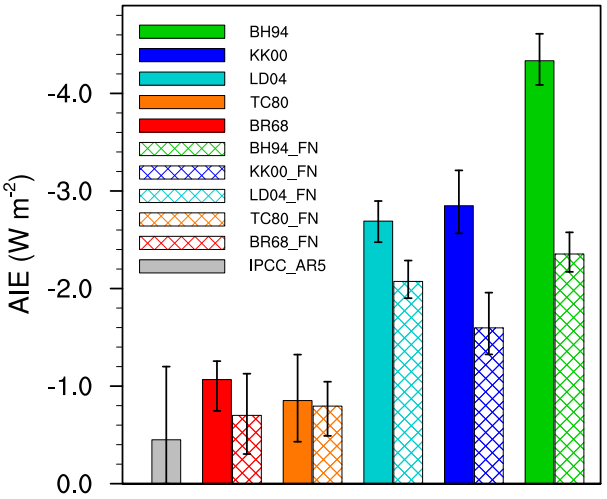

FIG. 9. Global-mean PD − PI differences in AIE for the default (colored solid fill) and the fixed N_C (grid fill) simulations, as well as for expert judgement of IPCC AR5 (gray solid fill). The error bars indicate the maximum and minimum annual mean values during the 11-yr simulations and the uncertainty range of IPCC AR5 judgment.

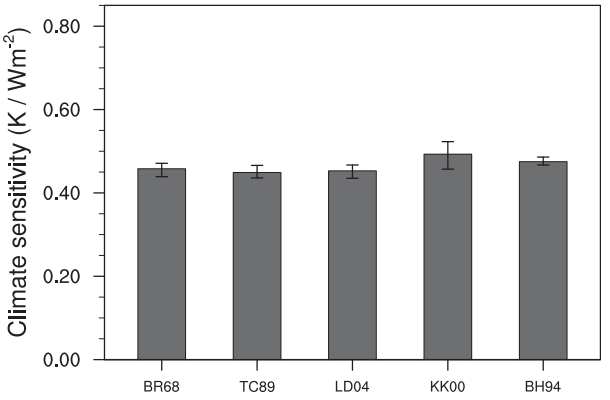

FIG. 10. Climate sensitivities of the MIROC5.2 model with the various autoconversion schemes derived with the method of Cess et al. (1990). The error bars indicate the maximum and minimum annual mean values during the 6-yr runs.

relatively small, mostly within the uncertainty range of the IPCC AR5 judgement. Both ΔLWP (Fig. 11b) and ΔCDNC (Fig. 11c) are substantially suppressed for KK00 and BH94 when a small β is used. One exception is LD04, which gives an AIE as large as $\sim$1.9 W m^{-2} with $\beta = -1/3$. One major difference between the LD04 scheme and others is the use of a R_e threshold that varies with L_c and N_c. If the R_e threshold is eliminated from the default LD04 formulation, it yields the AIE (with $\beta = -1$) much closer to BR68 which also has $\beta = \sim -1$, implying that the appropriate use of warm rain onset threshold can mitigate the effect of the β used.

The BR68 and TC80 schemes both show a relatively larger AIE sensitivity to the increase of β (more negative): a small increase in β (BR68: from ~ -1 to ~ -1.2, TC80: from $-1/3$ to $-2/3$) takes the magnitudes of AIE comparable to those of the schemes with larger β. These are largely related to the high sensitivity of ΔCDNC to β of the two schemes (Fig. 11c).

These results suggest that β, which largely determines the susceptibility of warm rain formation to aerosol perturbations in the first place, significantly influences the AIE via its modulation to cloud property responses. Meanwhile, the choice of rain onset threshold can potentially mitigate the effect of β.

c. *Effect of wet scavenging feedback*

This subsection extends the exploration of the wet scavenging feedback on AIE found by JS18 to multiple autoconversion schemes. The discrepancies in S_{wscv} as shown in Fig. 5 result in significantly different PD − PI AOD differences (ΔAOD; Fig. 12) among the various autoconversion schemes. These differences in ΔAOD feed back onto and contribute partly to cloud water (Figs. 7 and 8) and AIE (Fig. 6): larger aerosol loadings provide extra cloud condensation nuclei (CCN), which further inhibit rain formation and enlarge ΔLWP, ΔCDNC, and AIE. As described in section 2c, the experiments of "fixed N_c for wet scavenging + interactive N_c for cloud microphysics" are conducted to estimate the contribution of the wet scavenging feedback onto ΔLWP and AIE.

The resultant global-mean AIEs that exclude wet scavenging feedbacks are shown in Fig. 9 (grid fill); similarly, the global-mean ΔLWP and ΔAOD are shown in Fig. 13. The AIEs for the fixed-N_c experiments (denoted as "_FN") are all smaller than the corresponding default experiments, implying that the amplification effect of wet scavenging feedback pointed out by JS18 applies to all the autoconversion schemes examined. BH94 shows the largest differences in AIE between the default and the fixed-N_c experiments, while TC80 shows the smallest; this is also consistent with the finding of JS18 that schemes that represent both nonprecipitating and precipitating RR profiles in CFODDs (e.g., BH94, KK00, and LD04; Fig. 2) closer to satellite observations tend to have larger wet scavenging feedback. The scheme-dependent importance of wet scavenging feedback is also clearly shown in Fig. 13: the ΔLWPs and ΔAOD values for the BH94_FN, KK00_FN, and LD04_FN experiments are generally reduced from their default experiments to an extent larger than the other two schemes. The wet scavenging feedback is thus a critical pathway through which the precipitation schemes can influence the simulated Earth energy budget, particularly for those that feature impeded (observation-like) rain formation at small droplet sizes.

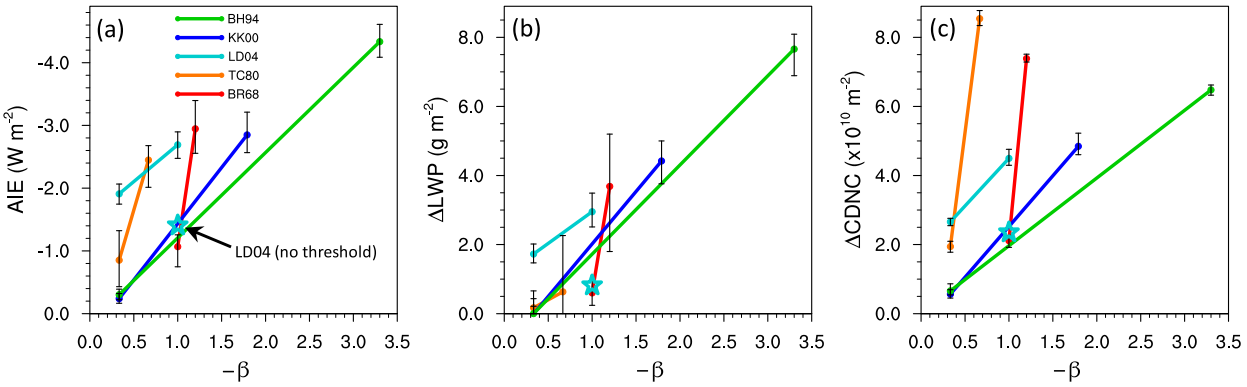

FIG. 11. The (a) AIE and PD − PI differences in (b) LWP and (c) CDNC simulated by the five autoconversion schemes, each with its default and a designated value of β. The error bars indicate the maximum and minimum annual mean values. The stars show the results of LD04 without using the R_e threshold.

To summarize, Fig. 14 demonstrates the key role of process-level behavior of precipitation in modulating the liquid water and aerosol loading responses to emission perturbations, and hence the AIE. For a given amount of increase in aerosol emissions (i.e., from PI to PD), schemes with larger S_P, which is controlled largely by the form of the autoconversion formulation (i.e., the value of β and the threshold setup), tend to yield larger

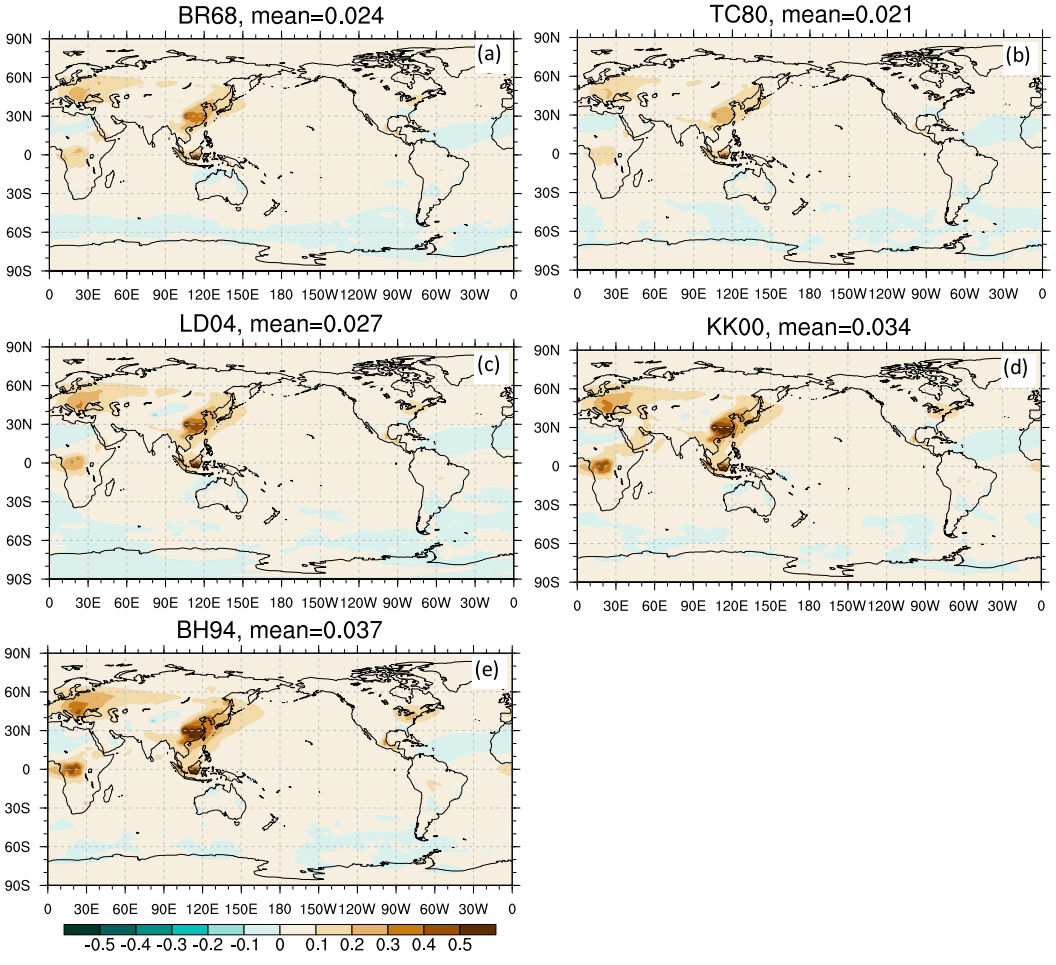

FIG. 12. As in Fig. 6, but for the PD − PI differences in AOD (ΔAOD).

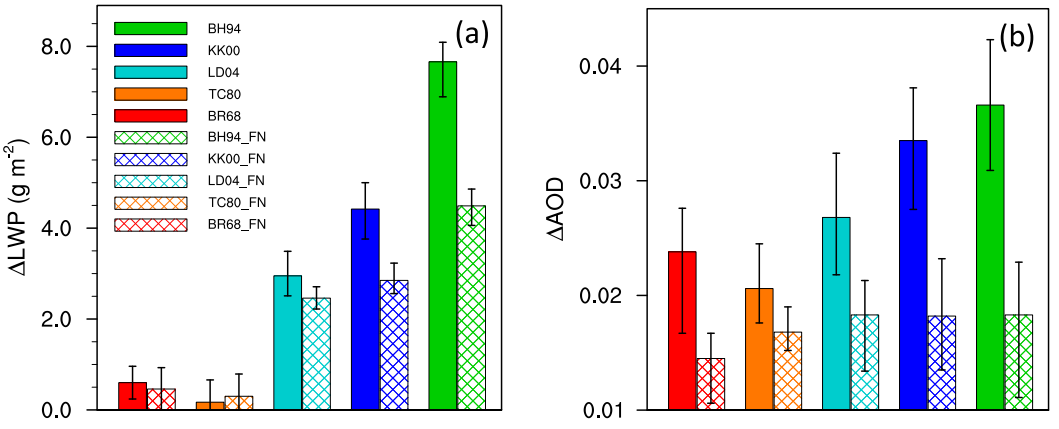

FIG. 13. As in Fig. 9, but for (a) ΔLWP and (b) ΔAOD.

LWP responses and also larger AOD increases; the latter interplays with and contributes to the former through the positive feedback involving rain formation and wet scavenging. These jointly result in more pronounced AIEs for schemes with larger S_P.

5. Conclusions and discussion

Precipitation parameterizations are a key source of uncertainties in climate simulations. Many studies have been endeavoring to constrain the precipitation formation process with observations. A common bias has been identified in many state-of-the-art GCMs: precipitation, especially in the form of warm rains, is triggered more frequently than revealed from observations. In this study, five different autoconversion schemes were implemented into a single GCM to systematically investigate the impact of the autoconversion formulations on the process-level behavior of warm rain formation in comparison with the A-Train observations, and to examine their effects on the simulated PI-to-PD AIE.

It was found that the too-frequent warm rain bias was mitigated by some schemes due to the inhibited rain formation under conditions of small droplet sizes such as in polluted regions, consistent with satellite observations. These better representations of warm rain formation were associated with the formulations of autoconversion, particularly the power-law dependence upon N_c (i.e., the β in $R_{\text{aut}} \propto L_c^{\alpha} N_c^{\beta}$). Specifically, the use of larger (more negative) β was found to exert larger precipitation susceptibilities to aerosol perturbations, which led to more nonprecipitating clouds in aerosol-rich environments. In contrast, schemes with smaller (less negative) β tended to feature much smaller precipitation susceptibilities to aerosols and severely overestimated warm rain occurrence frequencies. The appropriate use of rain onset threshold can mitigate the effect of β. These process-level discrepancies played a crucial role in modulating the simulated AIEs from the PI to the PD

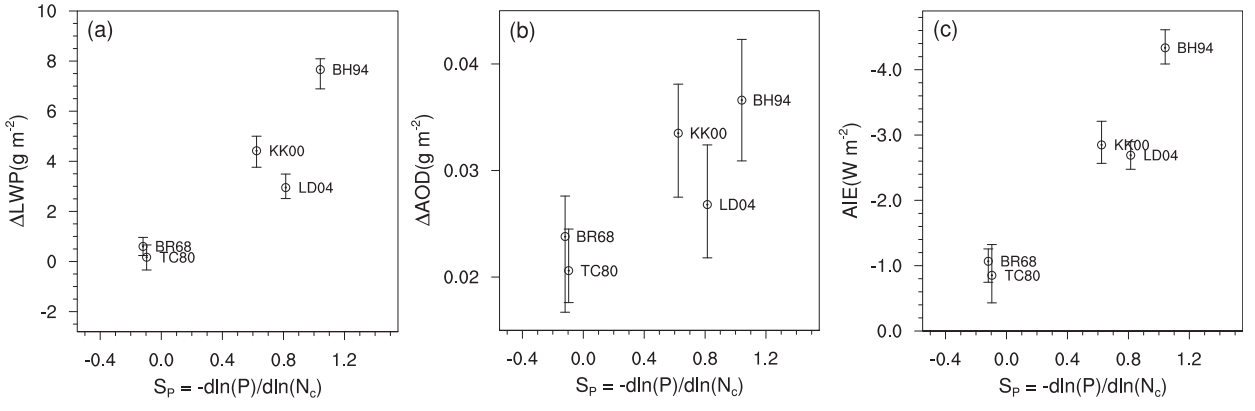

FIG. 14. The relationship between the mean surface precipitation susceptibilities S_P weighted with available cloud water amount (bin width × probability for each LWP bin) over the LWP bins and the (a) ΔLWP, (b) ΔAOD, and (c) AIE. The error bars indicate the maximum and minimum annual mean values during the 11-yr simulations.

periods: schemes that are inclined to significantly inhibit rain formation with increasing aerosols showed much larger AIEs than did the ones that hardly inhibited rain formation.

The plausible improvements in the warm rain formation process (i.e., inhibited rain formation) caused too large (negative) AIEs that could cancel much of the warming trend since the beginning of industrial era. That is, the bottom-up constraint on the precipitation formation process acts contrary to the top-down energy budget requirement for AIE, implying that compensating errors exist between the precipitation process and other parts of the model, such as the wet scavenging process (Garrett et al. 2006; Bourgeois and Bey 2011; Ohata et al. 2016), that require more targeted investigations and constraints.

It is worth noting that satellite-based constraints on model microphysics suffer from uncertainties, originating from the measurement and retrieval errors and limitations inherent in observational data (Ma et al. 2018) and also the scale disparity between observation and model resolutions (Feingold et al. 2016). Even though the use of COSP can limit the above uncertainties to the largest extent, the subgrid assumptions applied in COSP are not free from problems (Song et al. 2018). With these considerations, the top-down emergent constraints on AIE that seek robust and observable patterns of aerosol–cloud relationship on a larger scale (Klein and Hall 2015) may provide complementary information for model evaluation. In a particular model analyzed here, the bottom-up and top-down constraints may be combined primarily over regions with the largest AIEs: first, the anthropogenic source regions over land, where precipitation is very likely associated with ice- or mixed-phase clouds (Mülmenstädt et al. 2015), and second, the surrounding oceans where thinner marine stratocumulus prevails (Bulatovic et al. 2019).

Acknowledgments. This study was supported by NOAA's Climate Program Office's Modeling, Analysis, Predictions and Projections program with Grant NA15OAR4310153. K.S. was also supported by the JAXA EarthCARE and GCOM-C projects and the Integrated Research Program for Advancing Climate Models (TOUGOU program) from the Ministry of Education, Culture, Sports, Science and Technology (MEXT), Japan.

REFERENCES

Abdul-Razzak, H., and S. J. Ghan, 2000: A parameterization of aerosol activation: 2. Multiple aerosol types. *J. Geophys. Res.*, **105**, 6837–6844, https://doi.org/10.1029/1999JD901161.

Adler, R. F., and Coauthors, 2003: The version 2 Global Precipitation Climatology Project (GPCP) Monthly Precipitation Analysis (1979–present). *J. Hydrometeor.*, **4**, 1147–1167, https://doi.org/10.1175/1525-7541(2003)004<1147:TVGPCP>2.0.CO;2.

Albrecht, B. A., 1989: Aerosols, cloud microphysics, and fractional cloudiness. *Science*, **245**, 1227–1230, https://doi.org/10.1126/science.245.4923.1227.

Bai, H., C. Gong, M. Wang, Z. Zhang, and T. L'Ecuyer, 2018: Estimating precipitation susceptibility in warm marine clouds using multi-sensor aerosol and cloud products from A-Train satellites. *Atmos. Chem. Phys.*, **18**, 1763–1783, https://doi.org/10.5194/acp-18-1763-2018.

Beheng, K. D., 1994: A parameterization of warm cloud microphysical conversion processes. *Atmos. Res.*, **33**, 193–206, https://doi.org/10.1016/0169-8095(94)90020-5.

Berry, E. X., 1968: Modification of the warm rain process. *Proc. First Conf. on Weather Modification*, Albany, NY, Amer. Meteor. Soc., 81–85.

Boers, R., J. B. Jensen, and P. B. Krummel, 1998: Microphysical and short-wave radiative structure of stratocumulus clouds over the Southern Ocean: Summer results and seasonal differences. *Quart. J. Roy. Meteor. Soc.*, **124**, 151–168, https://doi.org/10.1002/qj.49712454507.

Boucher, O., and Coauthors, 2013: Clouds and aerosols. *Climate Change 2013: The Physical Science Basis*, T. F. Stocker et al., Eds., Cambridge University Press, 571–657.

Bourgeois, Q., and I. Bey, 2011: Pollution transport efficiency toward the Arctic: Sensitivity to aerosol scavenging and source regions. *J. Geophys. Res.*, **116**, D08213, https://doi.org/10.1029/2010JD015096.

Bulatovic, I., A. M. L. Ekman, J. Savre, I. Riipinen, and C. Leck, 2019: Aerosol indirect effects in marine stratocumulus: The importance of explicitly predicting cloud droplet activation. *Geophys. Res. Lett.*, **46**, 3473–3481, https://doi.org/10.1029/2018GL081746.

Cess, R. D., and Coauthors, 1990: Intercomparison and interpretation of climate feedback processes in 19 atmospheric general circulation models. *J. Geophys. Res.*, **95**, 16 601–16 615, https://doi.org/10.1029/JD095iD10p16601.

Collins, M., and Coauthors, 2013: Long-term climate change: Projections, commitments and irreversibility. *Climate Change 2013: The Physical Science Basis*, T. F. Stocker et al., Eds., Cambridge University Press, 1029–1136.

Donner, L., T. O'Brien, D. Rieger, B. Vogel, and W. F. Cooke, 2016: Are atmospheric updrafts a key to unlocking climate forcing and sensitivity? *Atmos. Chem. Phys.*, **16**, 12 983–12 992, https://doi.org/10.5194/acp-16-12983-2016.

Elsaesser, G. S., C. W. O'Dell, M. D. Lebsock, R. Bennartz, T. J. Greenwald, and F. J. Wentz, 2017: The Multisensor Advanced Climatology of Liquid Water Path (MAC-LWP). *J. Climate*, **30**, 10 193–10 210, https://doi.org/10.1175/JCLI-D-16-0902.1.

Fan, J., R. Leung, D. Rosenfeld, Q. Chen, Z. Li, J. Zhang, and H. Yan, 2013: Microphysical effects determine macrophysical response for aerosol impacts on deep convective clouds. *Proc. Natl. Acad. Sci. USA*, **110**, E4581–E4590, https://doi.org/10.1073/pnas.1316830110.

Feingold, G., A. McComiskey, D. Rosenfeld, and A. Sorooshian, 2013: On the relationship between cloud contact time and precipitation susceptibility to aerosol. *J. Geophys. Res. Atmos.*, **118**, 10 544–10 554, https://doi.org/10.1002/jgrd.50819.

——, ——, T. Yamaguchi, J. S. Johnson, K. S. Carslaw, and K. S. Schmidt, 2016: New approaches to quantifying aerosol influence

on the cloud radiative effect. *Proc. Natl. Acad. Sci. USA*, **113**, 5812–5819, https://doi.org/10.1073/pnas.1514035112.

Garrett, T. J., L. Avey, P. I. Palmer, A. Stohl, J. A. Neuman, C. A. Brock, T. B. Ryerson, and J. S. Holloway, 2006: Quantifying wet scavenging processes in aircraft observations of nitric acid and cloud condensation nuclei. *J. Geophys. Res.*, **111**, D23S51, https://doi.org/10.1029/2006JD007416.

Ghan, S., 2013: Estimating aerosol effects on cloud radiative forcing. *Atmos. Chem. Phys.*, **13**, 9971–9974, https://doi.org/10.5194/acp-13-9971-2013.

——, and Coauthors, 2016: Challenges in constraining anthropogenic aerosol effects on cloud radiative forcing using present-day spatiotemporal variability. *Proc. Natl. Acad. Sci. USA*, **113**, 5804–5811, https://doi.org/10.1073/pnas.1514036113.

Golaz, J.-C., M. Salzmann, L. Donner, L. Horowitz, Y. Ming, and M. Zhao, 2011: Sensitivity of the aerosol indirect effect to subgrid variability in the cloud parameterization of the GFDL atmosphere general circulation model AM3. *J. Climate*, **24**, 3145–3160, https://doi.org/10.1175/2010JCLI3945.1.

——, L. W. Horowitz, and H. Levy II, 2013: Cloud tuning in a coupled climate model: Impact on 20th century warming. *Geophys. Res. Lett.*, **40**, 2246–2251, https://doi.org/10.1002/grl.50232.

Grosvenor, D. P., and Coauthors, 2018: Remote sensing of droplet number concentration in warm clouds: A review of the current state of knowledge and perspectives. *Rev. Geophys.*, **56**, 409–453, https://doi.org/10.1029/2017RG000593.

Hansen, J., and Coauthors, 2005: Efficacy of climate forcings. *J. Geophys. Res.*, **110**, D18104, https://doi.org/10.1029/2005JD005776.

Hartmann, D. L., and Coauthors, 2013: Observations: Atmosphere and surface. *Climate Change 2013: The Physical Science Basis*, T. F. Stocker et al., Eds., Cambridge University Press, 159–254.

Haynes, J. M., R. T. Marchand, Z. Luo, A. Boda-Salcedo, and G. L. Stephens, 2007: A multipurpose radar simulation package: Quickbeam. *Bull. Amer. Meteor. Soc.*, **88**, 1723–1727, https://doi.org/10.1175/BAMS-88-11-1723.

——, T. L'Ecuyer, G. L. Stephens, S. D. Miller, C. Mitrescu, N. B. Wood, and S. Tanelli, 2009: Rainfall retrievals over the ocean with spaceborne high-frequency cloud radar. *J. Geophys. Res.*, **114**, D00A22, https://doi.org/10.1029/2008JD009973.

Hill, A. A., B. J. Shipway, and I. A. Boutle, 2015: How sensitive are aerosol–precipitation interactions to the warm rain representation? *J. Adv. Model. Earth Syst.*, **7**, 987–1004, https://doi.org/10.1002/2014MS000422.

Jiang, H., G. Feingold, and A. Sorooshian, 2010: Effect of aerosol on the susceptibility and efficiency of precipitation in warm trade cumulus clouds. *J. Atmos. Sci.*, **67**, 3525–3540, https://doi.org/10.1175/2010JAS3484.1.

Jing, X., and K. Suzuki, 2018: The impact of process-based warm rain constraints on the aerosol indirect effect. *Geophys. Res. Lett.*, **45**, 10 729–10 737, https://doi.org/10.1029/2018GL079956.

——, ——, H. Guo, D. Goto, T. Ogura, T. Koshiro, and J. Mülmenstädt, 2017: A multimodel study on warm precipitation biases in global models compared to satellite observations. *J. Geophys. Res. Atmos.*, **122**, 11 806–11 824, https://doi.org/10.1002/2017JD027310.

Kaufman, Y., and I. Koren, 2006: Smoke and pollution aerosol effect on cloud cover. *Science*, **313**, 655–658, https://doi.org/10.1126/science.1126232.

Kay, J. E., T. L'Ecuyer, A. Pendergrass, H. Chepfer, R. Guzman, and V. Yettella, 2018: Scale-aware and definition-aware evaluation of modeled near-surface precipitation frequency using CloudSat observations. *J. Geophys. Res.*, **123**, 4294–4309, https://doi.org/10.1002/2017JD028213.

Khairoutdinov, M., and Y. Kogan, 2000: A new cloud physics parameterization in a large-eddy simulation model of marine stratocumulus. *Mon. Wea. Rev.*, **128**, 229–243, https://doi.org/10.1175/1520-0493(2000)128<0229:ANCPPI>2.0.CO;2.

Klein, S. A., and A. Hall, 2015: Emergent constraints for cloud feedbacks. *Curr. Climate Change Rep.*, **1**, 276–287, https://doi.org/10.1007/s40641-015-0027-1.

Knutti, R., T. Stocker, F. Joos, and G.-K. Plattner, 2002: Constraints on radiative forcing and future climate change from observations and climate model ensembles. *Nature*, **416**, 719–723, https://doi.org/10.1038/416719a.

Lin, J., T. Qian, and T. Shinoda, 2014: Stratocumulus clouds in southeastern Pacific simulated by eight CMIP5–CFMIP global climate models. *J. Climate*, **27**, 3000–3022, https://doi.org/10.1175/JCLI-D-13-00376.1.

Liu, Y., and P. H. Daum, 2004: Parameterization of the autoconversion process. Part I: Analytical formulation of the Kessler-type parameterizations. *J. Atmos. Sci.*, **61**, 1539–1548, https://doi.org/10.1175/1520-0469(2004)061<1539:POTAPI>2.0.CO;2.

Loeb, N. G., and Coauthors, 2018: Clouds and the Earth's Radiant Energy System (CERES) Energy Balanced and Filled (EBAF) top-of-atmosphere (TOA) edition 4.0 data product. *J. Climate*, **31**, 895–918, https://doi.org/10.1175/JCLI-D-17-0208.1.

Ma, P.-L., P. Rasch, H. Chepfer, D. Winker, and S. Ghan, 2018: Observational constraint on cloud susceptibility weakened by aerosol retrieval limitations. *Nat. Commun.*, **9**, 2640, https://doi.org/10.1038/s41467-018-05028-4.

Malavelle, F., and Coauthors, 2017: Strong constraints on aerosol–cloud interactions from volcanic eruptions. *Nature*, **546**, 485–491, https://doi.org/10.1038/nature22974.

Marchand, R., G. G. Mace, T. Ackerman, and G. Stephens, 2008: Hydrometeor detection using *Cloudsat*—An Earth-orbiting 94-GHz cloud radar. *J. Atmos. Oceanic Technol.*, **25**, 519–533, https://doi.org/10.1175/2007JTECHA1006.1.

Michibata, T., and T. Takemura, 2015: Evaluation of autoconversion schemes in a single model framework with satellite observations. *J. Geophys. Res.*, **120**, 9570–9590, https://doi.org/10.1002/2015JD023818.

——, K. Suzuki, Y. Sato, and T. Takemura, 2016: The source of discrepancies in aerosol–cloud–precipitation interactions between GCM and A-Train retrievals. *Atmos. Chem. Phys.*, **16**, 15 413–15 424, https://doi.org/10.5194/acp-16-15413-2016.

——, ——, M. Sekiguchi, and T. Takemura, 2019: Prognostic precipitation in the MIROC6-SPRINTARS GCM: Description and evaluation against satellite observations. *J. Adv. Model. Earth Syst.*, **11**, 839–860, https://doi.org/10.1029/2018MS001596.

Mülmenstädt, J., O. Sourdeval, J. Delanoë, and J. Quaas, 2015: Frequency of occurrence of rain from liquid-, mixed-, and ice-phase clouds derived from A-Train satellite retrievals. *Geophys. Res. Lett.*, **42**, 6502–6509, https://doi.org/10.1002/2015GL064604.

Myhre, G., and Coauthors, 2013: Anthropogenic and natural radiative forcing. *Climate Change 2013: The Physical Science Basis*, T. F. Stocker et al., Eds., Cambridge University Press, 659–740.

Nakajima, T. Y., K. Suzuki, and G. L. Stephens, 2010: Droplet growth in warm water clouds observed by the A-Train. Part II: A multisensor view. *J. Atmos. Sci.*, **67**, 1897–1907, https://doi.org/10.1175/2010JAS3276.1.

Norris, J. R., R. J. Allen, A. T. Evan, M. D. Zelinka, C. W. O'Dell, and S. A. Klein, 2016: Evidence for climate change in the satellite cloud record. *Nature*, **536**, 72–75, https://doi.org/10.1038/nature18273.

Ohata, S., N. Moteki, T. Mori, M. Koike, and Y. Kondo, 2016: A key process controlling the wet removal of aerosols: New observational evidence. *Sci. Rep.*, **6**, 34113, https://doi.org/10.1038/srep34113.

Pawlowska, H., and J.-L. Brenguier, 2003: An observational study of drizzle formation in stratocumulus clouds for general circulation model (GCM) parameterizations. *J. Geophys. Res.*, **108**, 8630, https://doi.org/10.1029/2002JD002679.

Pincus, R., S. Platnick, S. A. Ackerman, R. S. Hemler, and R. J. P. Hofmann, 2012: Reconciling simulated and observed views of clouds: MODIS, ISCCP, and the limits of instrument simulators. *J. Climate*, **25**, 4699–4720, https://doi.org/10.1175/JCLI-D-11-00267.1.

Platnick, S., S. A. Ackerman, M. D. King, K. Meyer, W. P. Menzel, R. E. Holz, B. A. Baum, and P. Yang, 2015: MODIS atmosphere L2 cloud product (06_L2), NASA MODIS Adaptive Processing System. Goddard Space Flight Center, accessed 12 November 2018, https://doi.org/10.5067/MODIS/MOD06_L2.006.

——, and Coauthors, 2017: The MODIS cloud optical and microphysical products: Collection 6 updates and examples from Terra and Aqua. *IEEE Trans. Geosci. Remote Sens.*, **55**, 502–525, https://doi.org/10.1109/TGRS.2016.2610522.

Posselt, R., and U. Lohmann, 2009: Sensitivity of the total anthropogenic aerosol effect to the treatment of rain in a global climate model. *Geophys. Res. Lett.*, **36**, L02805, https://doi.org/10.1029/2008GL035796.

Rosenfeld, D., and Coauthors, 2014: Global observations of aerosol–cloud–precipitation–climate interactions. *Rev. Geophys.*, **52**, 750–808, https://doi.org/10.1002/2013RG000441.

Rothenberg, D., A. Avramov, and C. Wang, 2018: On the representation of aerosol activation and its influence on model-derived estimates of the aerosol indirect effect. *Atmos. Chem. Phys.*, **18**, 7961–7983, https://doi.org/10.5194/acp-18-7961-2018.

Rotstayn, L. D., 2000: On the "tuning" of autoconversion parameterizations in climate models. *J. Geophys. Res.*, **105**, 15 495–15 507, https://doi.org/10.1029/2000JD900129.

——, M. A. Collier, D. T. Shindell, and O. Boucher, 2015: Why does aerosol forcing control historical global-mean surface temperature change in CMIP5 models? *J. Climate*, **28**, 6608–6625, https://doi.org/10.1175/JCLI-D-14-00712.1.

Small, J. D., P. Y. Chuang, G. Feingold, and H. Jiang, 2009: Can aerosol decrease cloud lifetime? *Geophys. Res. Lett.*, **36**, L16806, https://doi.org/10.1029/2009GL038888.

Song, H., Z. Zhang, P.-L. Ma, S. Ghan, and M. Wang, 2018: The importance of considering sub-grid cloud variability when using satellite observations to evaluate the cloud and precipitation simulations in climate models. *Geosci. Model Dev.*, **11**, 3147–3158, https://doi.org/10.5194/gmd-11-3147-2018.

Sorooshian, A., G. Feingold, M. Lebsock, H. Jiang, and G. Stephens, 2009: On the precipitation susceptibility of clouds to aerosol perturbations. *Geophys. Res. Lett.*, **36**, L13803, https://doi.org/10.1029/2009GL038993.

Stephens, G. L., and Coauthors, 2008: CloudSat mission: Performance and early science after the first year of operation. *J. Geophys. Res.*, **113**, D00A18, https://doi.org/10.1029/2008JD009982.

——, and Coauthors, 2010: Dreary state of precipitation in global models. *J. Geophys. Res.*, **115**, D24211, https://doi.org/10.1029/2010JD014532.

——, D. Winker, J. Pelon, C. Trepte, D. Vane, C. Yuhas, T. L'Ecuyer, and M. Lebsock, 2018: CloudSat and CALIPSO within the A-Train: Ten years of actively observing the Earth system. *Bull. Amer. Meteor. Soc.*, **99**, 569–581, https://doi.org/10.1175/BAMS-D-16-0324.1.

Stevens, B., 2015: Rethinking the lower bound on aerosol radiative forcing. *J. Climate*, **28**, 4794–4819, https://doi.org/10.1175/JCLI-D-14-00656.1.

——, and G. Feingold, 2009: Untangling aerosol effects on clouds and precipitation in a buffered system. *Nature*, **461**, 607–613, https://doi.org/10.1038/nature08281.

Sullivan, R. C., P. Crippa, H. Matsui, R. L. Leung, C. Zhao, A. Thota, and S. C. Pryor, 2018: New particle formation leads to cloud dimming. *npj Climate Atmos. Sci.*, **1**, 9, https://doi.org/10.1038/s41612-018-0019-7.

Suzuki, K., T. Y. Nakajima, and G. L. Stephens, 2010: Particle growth and drop collection efficiency of warm clouds as inferred from joint CloudSat and MODIS observations. *J. Atmos. Sci.*, **67**, 3019–3032, https://doi.org/10.1175/2010JAS3463.1.

——, G. L. Stephens, S. C. van den Heever, and T. Y. Nakajima, 2011: Diagnosis of the warm rain process in cloud-resolving models using joint CloudSat and MODIS observations. *J. Atmos. Sci.*, **68**, 2655–2670, https://doi.org/10.1175/JAS-D-10-05026.1.

——, J.-C. Golaz, and G. L. Stephens, 2013: Evaluating cloud tuning in a climate model with satellite observations. *Geophys. Res. Lett.*, **40**, 4464–4468, https://doi.org/10.1002/grl.50874.

——, G. L. Stephens, A. Bodas-Salcedo, M. Wang, J.-C. Golaz, T. Yokohata, and T. Koshiro, 2015: Evaluation of the warm rain formation process in global models with satellite observations. *J. Atmos. Sci.*, **72**, 3996–4014, https://doi.org/10.1175/JAS-D-14-0265.1.

——, ——, and J. C. Golaz, 2017: Significance of aerosol radiative effect in energy balance control on global precipitation change. *Atmos. Sci. Lett.*, **18**, 389–395, https://doi.org/10.1002/asl.780.

Swales, D. J., R. Pincus, and A. Bodas-Salcedo, 2018: The Cloud Feedback Model Intercomparison Project Observational Simulator Package: Version 2. *Geosci. Model Dev.*, **11**, 77–81, https://doi.org/10.5194/gmd-11-77-2018.

Takahashi, H., K. Suzuki, and G. Stephens, 2017: Land–ocean differences in the warm-rain formation process in satellite and ground-based observations and model simulations. *Quart. J. Roy. Meteor. Soc.*, **143**, 1804–1815, https://doi.org/10.1002/qj.3042.

Takemura, T., H. Okamoto, Y. Maruyama, A. Numaguti, A. Higurashi, and T. Nakajima, 2000: Global three-dimensional simulation of aerosol optical thickness distribution of various origins. *J. Geophys. Res.*, **105**, 17 853–17 873, https://doi.org/10.1029/2000JD900265.

——, T. Nakajima, O. Dubovik, B. Holben, and S. Kinne, 2002: Single-scattering albedo and radiative forcing of various aerosol species with a global three-dimensional model. *J. Climate*, **15**, 333–352, https://doi.org/10.1175/1520-0442(2002)015<0333:SSAARF>2.0.CO;2.

——, M. Egashira, K. Matsuzawa, H. Ichijo, R. O'ishi, and A. Abe-Ouchi, 2009: A simulation of the global distribution and radiative forcing of soil dust aerosols at the Last Glacial Maximum. *Atmos. Chem. Phys.*, **9**, 3061–3073, https://doi.org/10.5194/acp-9-3061-2009.

Textor, C., and Coauthors, 2006: Analysis and quantification of the diversities of aerosol life cycles within AeroCom. *Atmos.*

Chem. Phys., **6**, 1777–1813, https://doi.org/10.5194/acp-6-1777-2006.

Tripoli, G., and W. Cotton, 1980: A numerical investigation of several factors contributing to the observed variable intensity of deep convection over south Florida. *J. Appl. Meteor.*, **19**, 1037–1063, https://doi.org/10.1175/1520-0450(1980)019<1037:ANIOSF>2.0.CO;2.

Tsushima, Y., and Coauthors, 2017: The Cloud Feedback Model Intercomparison Project (CFMIP) diagnostic codes catalogue—Metrics, diagnostics and methodologies to evaluate, understand and improve the representation of clouds and cloud feedbacks in climate models. *Geosci. Model Dev.*, **10**, 4285–4305, https://doi.org/10.5194/gmd-10-4285-2017.

Twomey, S., 1977: Influence of pollution on shortwave albedo of clouds. *J. Atmos. Sci.*, **34**, 1149–1152, https://doi.org/10.1175/1520-0469(1977)034<1149:TIOPOT>2.0.CO;2.

van Vuuren, D. P., and Coauthors, 2011: The representative concentration pathways: An overview. *Climatic Change*, **109**, 5–31, https://doi.org/10.1007/s10584-011-0148-z.

Wang, M., and Coauthors, 2012: Constraining cloud lifetime effects of aerosols using A-Train satellite observations. *Geophys. Res. Lett.*, **39**, L15709, https://doi.org/10.1029/2012GL052204.

Watanabe, M., and Coauthors, 2010: Improved climate simulation by MIROC5: Mean states, variability, and climate sensitivity. *J. Climate*, **23**, 6312–6335, https://doi.org/10.1175/2010JCLI3679.1.

Wilcox, L. J., E. J. Highwood, and N. J. Dunstone, 2013: The influence of anthropogenic aerosol on multi-decadal variations of historical global climate. *Environ. Res. Lett.*, **8**, 024033, https://doi.org/10.1088/1748-9326/8/2/024033.

Zhang, H., S. Zhao, Z. Wang, X. Zhang, and L. Song, 2016: The updated effective radiative forcing of major anthropogenic aerosols and their effects on global climate at present and in the future. *Int. J. Climatol.*, **36**, 4029–4044, https://doi.org/10.1002/joc.4613.

Zhao, M., and Coauthors, 2016: Uncertainty in model climate sensitivity traced to representations of cumulus precipitation microphysics. *J. Climate*, **29**, 543–560, https://doi.org/10.1175/JCLI-D-15-0191.1.